Annual ecosystem variability in the tropical Indian Ocean: Results of a coupled bio-physical ocean general circulation model

J.D. Wiggert[a,b,*], R.G. Murtugudde[b], J.R. Christian[c,b]

[a]*Center for Coastal Physical Oceanography, Old Dominion University, Norfolk, VA 23508-2026, USA*
[b]*Earth System Science Interdisciplinary Center, University of Maryland, College Park, MD 20742-2465, USA*
[c]*Fisheries and Oceans Canada, Canadian Centre for Climate Modelling and Analysis, University of Victoria, Victoria, British Columbia, Canada V8W 2Y2*

Abstract

A coupled, 3-D bio-physical ocean general circulation model has been employed to study biogeochemical variability in the Indian Ocean. The model's ecosystem includes two size classes each of phytoplankton, zooplankton and detritus, and allows iron- and nitrogen-limited phytoplankton growth to develop. Comparison of SeaWiFS and modeled chlorophyll *a* demonstrates that the model successfully captures seasonal inter-regional contrasts in phytoplankton distribution. Model validation was performed against SeaWiFS ocean color, NODC nitrate, and US JGOFS observations from the Arabian Sea. These data were used to objectively evaluate several ecosystem model modifications that improved the solution. Phytoplankton speciation shifts were generally consistent with those observed in the Arabian Sea. The model shows pronounced basinwide spatio-temporal variability in iron availability; surface waters in the western equatorial and southern tropical regions always tend toward iron limitation, while the Bay of Bengal and the eastern Arabian Sea are largely iron replete. The model also indicates that surface waters in the western Arabian Sea are prone to seasonal iron limitation, despite proximity to regional dust sources. Phytoplankton blooms that manifest as a response to the Somali Current show better agreement with the SeaWiFS data than do previous modeling studies and biogeochemical variability associated with eastward propagation of the semiannual Wyrtki Jet is described for the first time. In the southern tropical region, the model indicates that austral winter Ekman pumping and westward propagating Rossby waves are the primary means of nutrient supply to these iron-limited waters. Finally, inter-regional connections associated with the propagation of the Somali Current and the Wyrtki Jet out of their respective source regions are shown to be a primary influence on seasonal biogeochemical variability in the southern Bay of Bengal. The results presented here establish a need for additional studies that apply such a basinwide approach to further advance our understanding of how bioavailable iron

*Corresponding author. Center for Coastal Physical Oceanography, Old Dominion University, Norfolk, VA, Canada 23508-2026, USA. Fax: +1 757 683 5550.

E-mail address: jwiggert@ccpo.odu.edu (J.D. Wiggert).

distribution, physical–biological interactions and inter-regional connections affect biogeochemical processes in the Indian Ocean.

1. Introduction

The Indian Ocean (IO) basin has two unique characteristics that fundamentally impact its biogeochemical processes. The first of these is the northern land boundary, which extends southward to at least 26 °N, with the Indian subcontinent dividing the Northern IO into the Arabian Sea in the west and the Bay of Bengal in the east. These geographical features preclude significant thermocline ventilation in the north and provide dust sources for elevated aeolian iron deposition. The second unique feature is the annual monsoon cycle, which is characterized by surface winds that reverse seasonally north of 10 °S and heavy precipitation over the northern half of the basin during boreal summer. The seasonal evolution of oceanic current patterns and upwelling distributions that develop in response to this forcing provide the physical framework that leads to pronounced biogeochemical variability throughout the basin.

The most prominent physical response to the northern hemisphere's reversing wind field occurs along the Arabian Sea's western boundary, where the Somali Current flows equatorward during the Northeast (winter) Monsoon (NEM) and poleward during the Southwest (summer) Monsoon (SWM). The character of oceanic upwelling in response to the two monsoon regimes also differs in the Arabian Sea. During the NEM, cool, dry northeasterly winds drive convective mixing well offshore that result in winter blooms of phytoplankton over the north and central Arabian Sea (Banse and McClain, 1986; Madhupratap et al., 1996; Wiggert et al., 2000). During the SWM, a combination of coastal upwelling, horizontal advection and Ekman pumping result in prominent phytoplankton blooms off the coasts of Oman (Brock and McClain, 1992; Latasa and Bidigare, 1998) and Somalia (Veldhuis et al., 1997; Hitchcock et al., 2000) that can propagate more than 500 km offshore.

The summer bloom off Somalia is associated with upwelled waters entrained around the Great Whirl,

an annually recurring anti-cyclonic circulation pattern that is the northern component of the Somali Current's two-gyre system (Schott, 1983; Fischer et al., 1996; Wirth et al., 2002). Its companion feature is the Southern Gyre, which typically manifests just north of the equator during the SWM (Schott and McCreary, 2001). In the Bay of Bengal, SWM-period Ekman pumping initiates the annually recurring cyclonic gyre known as the Sri Lanka Dome (Vinayachandran and Yamagata, 1998). Elevated biological activity is observed within both the Dome and the Southwest Monsoon Current (SMC) that advects around the Dome's southeast limb into the Bay of Bengal from the Arabian Sea (Vinayachandran et al., 2004). These two features combine to form the Bay's most prominent annually recurring biological signature. To the north, productivity in the Bay is impacted by the freshwater input from the rivers and has been linked to eddy activity (Kumar et al., 2004). In the equatorial IO, the thermocline is deeper in the east, where a 'warm pool' is maintained by the semi-annual transport associated with the eastward propagating Wyrtki Jets (Vinayachandran et al., 1999; Murtugudde et al., 2000). The structure of the equatorial thermocline (and nutricline) leads to prominent phytoplankton blooms in the west while biological activity in the east is relatively low and blooms typically do not extend far off the coast of Sumatra (although see Murtugudde et al., 1999). In the southern tropical IO (STIO), it has been demonstrated that satellite-observed surface Chl*a* variability is affected by westward propagating Rossby waves (Cipollini et al., 2001; Kawamiya and Oschlies, 2001).

Biogeochemical modeling studies of the IO to date have focused largely on the Arabian Sea. Two SWM-period studies employed simple biological formulations and demonstrated the importance of horizontal advection of waters upwelled along the Omani coast as a source of nutrients to the open ocean through the actions of offshore propagating jets and filaments (Young and Kindle, 1994; Keen

et al., 1997). McCreary et al. (1996) reported on the first attempt to simulate the Arabian Sea ecosystem's annual cycle. Their model successfully captured several prominent, annually recurring phytoplankton blooms, and featured pronounced mixed-layer detrainment blooms following both monsoon periods. The modeling study of Ryabchenko et al. (1998) had largely similar results. However, in the NE Arabian Sea neither effort captured the bloom observed by CZCS during the SWM, a failing that in both studies was primarily attributed to excessive grazing.

In more recent biogeochemical modeling studies, the importance of SWM-period nutrient advection for supporting the offshore phytoplankton blooms observed in the ocean-color data has been confirmed and the predominance of the northeast Somali and southwest Omani coasts as source regions has been demonstrated (Kawamiya, 2001). Mesoscale features, spawned by the vigorous monsoonal forcing, have been associated with episodic export flux events that are not resolved in the biogeochemical models that have so far appeared (Hood et al., 2003). Finally, the fundamental contribution of diel mixed-layer motions to the specific timing, magnitude and persistence of phytoplankton blooms during both monsoons has been established (Wiggert et al., 2000; McCreary et al., 2001; Wiggert et al., 2002). A comprehensive review of how these modeling studies have contributed to the evolution of our understanding of Arabian Sea biogeochemical variability appears in Wiggert et al. (2005).

The bio-physical model we employ has been recently applied in studies of annual and interannual variability of biogeochemical processes in the tropical Atlantic and Pacific Oceans (Christian et al., 2002a; Christian and Murtugudde, 2003; Wang et al., 2006). In this report, an analysis of a climatological solution for the IO north of 30°S is presented. To our knowledge, this is the first fully coupled physical–biogeochemical modeling study of the IO for which the basinwide biogeochemical dynamics are described, except for the carbon cycle model of Swathi et al. (2000) in which the domain extends to 15°S. The model ecosystem has nine components: large and small size classes of phytoplankton, zooplankton and detritus, and three nutrients (nitrate, ammonium and iron). The model successfully captures the basinwide contrast in phytoplankton abundance during the SWM. Significant new insights into the distribution of iron-limited surface waters indicated by the model and the influence of regional processes and inter-regional dynamical connections on seasonal biogeochemical variability throughout the basin are described. The appendix describes why several modifications to the ecosystem model's structure were implemented and how these improved the solution.

2. Methods

2.1. Description of the bio-physical OGCM

The physical model is a reduced gravity, primitive equation, sigma coordinate formulation that has been applied previously to the IO (Murtugudde and Busalacchi, 1999; Murtugudde et al., 2000). The spatial and seasonal characteristics of the model's temperature and salinity fields and mixed-layer dynamics have been validated and reported on in a previous analysis (Murtugudde and Busalacchi, 1999). The model employs an Arakawa A grid with a resolution of $1/2°$ (longitude) by $1/3°$ (latitude). Some of the model's principal features include a hybrid vertical mixing scheme (Chen et al., 1994) and coupling to an advective atmospheric mixed layer (Seager et al., 1995) that includes the determination of evaporation. Climatological precipitation was obtained from the Oberhuber (1998) atlas. Below the surface mixed layer are 19 sigma layers, with $\sigma = 0.0071, 0.0071, 0.0071, 0.0071, 0.0143, 0.0143, 0.0143, 0.0143, 0.0286, 0.0286, 0.0286, 0.0286, 0.0429, 0.0429, 0.0714, 0.0714, 0.1429, 0.2143, 0.2143$. The motionless deep layer is set at $9°C$ and 35 psu.

Surface wind stresses and wind speeds are daily mean climatology from the NCEP 40-year reanalysis (Kalnay et al., 1996). All other boundary conditions are based on monthly climatological data and their specific application to the OGCM has been described elsewhere (Murtugudde and Busalacchi, 1999; Christian et al., 2002a). Initial conditions for temperature and salinity are based on the climatological distribution (Antonov et al., 1998; Boyer et al., 1998). At the bottom boundary, the initial values of temperature, salinity, nitrate and iron are maintained. Along the southern boundary of the model domain, salinity, temperature and layer thickness are relaxed to seasonal climatological conditions between $25°S$ and $30°S$. The Indonesian Throughflow (ITF) and riverine inputs are not included in these experiments. The main run

climatological solution of the fully coupled bio-physical model discussed here was integrated for 16 years, with initial physical fields taken from a 30-year spin-up.

2.2. The ecosystem model

A nine-component oceanic ecosystem has been fully coupled to the physical OGCM and includes a large and small size class of phytoplankton (net-plankton and picoplankton), zooplankton (macro-zooplankton and microzooplankton) and detritus. Three nutrients (nitrate, ammonium and iron) also are included, along with explicit iron biogeochem-istry. Complete descriptions of the ecosystem model are provided in Leonard et al. (1999) and Christian et al. (2002a). The initial nitrate distribution was taken from the NODC climatology (Conkright et al., 1998). The iron initial condition was based on the nitrate distribution using two N:Fe ratios: 2.5×10^5 in the upper 135 m and 3×10^5 at greater depth. The surface N:Fe ratio was set at the threshold between nitrogen and iron limitation. The subsurface condition was based on the range of N:Fe ratios reported for upwelled waters off the Arabian Peninsula (Measures and Vink, 1999). These nutrient ratios were applied throughout the model domain. Iron solubility was increased to 750 pM (a value of 600 pM was previously applied), which reflects conditions in the IO (Saager et al., 1989; Takeda et al., 1995; Measures and Vink, 1999) and serves as an upper limit for subsurface iron concentrations. A consequence of the higher subsur-face N:Fe ratio and the solubility-imposed upper limit is that, without supplemental inputs, these waters will become iron limited if their nutrients are fully utilized. Thus, the degree that surface nutrient conditions tend toward nitrogen or iron limitation in the model depends on upwelling, atmospheric deposition and horizontal advection. Along the southern and eastern open boundaries, nitrate and iron were relaxed to the initial conditions. Atmo-spheric mineral dust concentrations used in creating estimates of aeolian iron deposition were taken from the GOCART atmospheric transport model (Ginoux et al., 2001).

Several modifications to the published version of the ecosystem model were made for this application to the IO. Nitrification occurs below an irradiance threshold ($5 \mu Ein/m^2/s$ at noon) rather than a fixed depth as in Christian et al. (2002a). The solubility of aeolian iron in seawater was lowered to 3% (from 10%), based on the findings of several recent studies (Jickells and Spokes, 2001, and references within). The iron initial and boundary conditions differ from the published simulations as noted above. We also have allowed zooplankton to graze on their corresponding size class of detritus, and the form of non-grazing mortality on the netplankton and macrozooplankton was modified. In order to assimilate these changes, some parameters were adjusted from those originally applied in the Equatorial Pacific (Christian et al., 2002a). The modified equations and parameter values, and a quantification of the impact of these modifications on the model solution are documented in the Appendix.

2.3. Surface chlorophyll a

Ocean-color satellites provide the only observa-tions of basin-scale biological variability. A seaso-nal climatology of surface chlorophyll a (Chla) has been created from SeaWiFS ocean-color data. The SeaWiFS data consists of continuous observations dating from September 1997 to January 2002. The climatology was determined using the level 3, monthly ocean-color data from the standard mapped images available through the Goddard DAAC (http://daac.gsfc.nasa.gov).

2.4. In situ validation of biogeochemical time series at regional sites

Twelve locations were chosen for comparing the solution to observational data (Fig. 1). These consist of five sites in the Arabian Sea (AS1–AS5), three sites in the Bay of Bengal (BB1–BB3), and two sites each in the equatorial IO (EQ1 and EQ2) and the STIO (ST1 and ST2). Site coordinates and their relevance to past studies are provided in Table 1. At all sites, time series of surface Chla and nitrate are compared to time series from the monthly SeaWiFS climatology and the seasonal NODC nitrate clima-tology (Conkright et al., 1998). Four of the five Arabian Sea extraction points in the model (AS1–AS4) coincide with standard stations occu-pied during the US JGOFS Arabian Sea Process Study (Smith et al., 1998b). Observations from these cruises provide a more complete characterization of spatio-temporal variation in plankton biomass and phytoplankton speciation over the monsoon cycle than has been available previously.
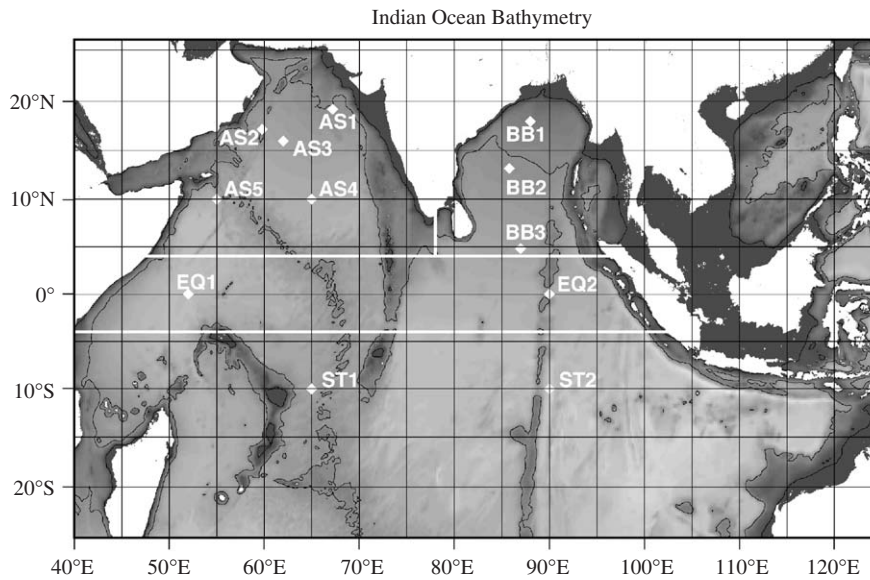
Indian Ocean Bathymetry

Fig. 1. Indian Ocean bathymetry obtained from the National Geophysical Data Center (http://www.ngdc.noaa.gov/ngdc.html), with the 200 m and 3000 m isobaths indicated with the additional contours. The twelve model extraction sites are shown. The site acronym used in this analysis is provided next to the symbol. Table 1 provides the coordinates and additional context pertaining to previous observational studies conducted in the vicinity of a given site. The white lines depict the boundaries of the four sub-regions defined in Section 2.5.

Table 1
Coordinates of model extraction sites

Site	Latitude	Longitude	Designation	Relevant literature
AS1	19.2 °N	67.2 °E	JGOFS N7	Smith et al.
AS2	17.2 °N	59.8 °E	JGOFS S4	(1998)
AS3	16 °N	62 °E	JGOFS S7	
AS4	10 °N	65 °E	JGOFS S15	
AS5	10 °N	55 °E	Somalia	
BB1	17.5 °N	88.5 °E	NBBT	Bhat et al.
BB2	13.2 °N	85.8 °E	CBBT	(2001), and
BB3	4.5 °N	87 °E	SBBT	Ramaswamy
				et al. (1994)
EQ1	0 °N	52 °E	IOZM (West)	Saji et al.
EQ2	0 °N	90 °E	IOZM (East)	(1999)
ST1	10 °S	65 °E	STIO (West)	
ST2	10 °S	90 °E	STIO (East)	

The designations for the four JGOFS sites are as they normally appear in the literature (e.g., Smith et al., 1998b). The designations for the three Bay of Bengal sites (NBBT, CBBT and SBBT) signify the northern/central/southern locations, respectively. These are consistent with the trap designations that appear in Ramaswamy and Nair (1994), though the precise location of the two northernmost extraction sites are compromises with the BOBMEX mooring locations (Bhat et al., 2001). The two equatorial sites (IOZM west and east) are within the boxes defined in Saji et al. (1999) that are used in their analysis of climate variability in the Indian Ocean. The Somalia site (AS5) and the two sites in the STIO (ST1 and ST2) have no present counterpart in the literature.

At these four JGOFS sites, primary production (PP), particulate organic nitrogen (PON), and zooplankton biomass from the process cruise profiles are included in the model/observation comparison (Table 2). To provide some perspective on the comparisons in the results to follow, the mean percentage differences for PP, PON and zooplankton biomass are 35%, 23% and 72%, respectively. Furthermore, zooplankton abundance from the observations of both Wishner et al. (1998) and Roman et al. (2000) are tabulated, and the percent difference between their co-located observations ranges up to 134%. The primary analyses that made use of the PP measurements and the PON measurements listed in Table 2 are those of Barber et al. (2001) and Gundersen et al. (1998), respectively. In addition, JGOFS observations of surface Chl*a* and nitrate supplement the standard validation data. At AS2–AS4 and BB1–BB3 model particle flux is compared to sediment trap time series from the Arabian Sea (Honjo et al., 1999) and the Bay of Bengal (Ramaswamy and Nair, 1994), respectively. Modeled export flux was extrapolated to depth using the Martin curve (Martin et al., 1987). Where sediment trap data are available the modeled flux is

Table 2
Observations are from JGOFS cruises TN043 (NEM), TN045 (SIM), TN049 (SWM) and TN053 (FIM/NEM)

Station	Season	PP (0–80 m) mMolC/m²/d		PON (0–100 m) mMolN/m²		Z_Wishner (0–100 m)	Z_Roman (0–100 m)	mMolN/m²
		US JGOFS	Model	US JGOFS	Model	US JGOFS		Model
AS1	NEM	103.1	93.1	46.8	65.3	8.7	11.5	8.9
(N7)	SIM	105.4	51.2	96.2	46.5	15.2	11.3	4.5
	SWM	76.7	78.2	48.7	49.5	*10.1*	*13.2*	7.1
	FIM/NEM	42.9	87.0	46.5	60.7	*9.0*	*nd*	10.1
AS2	NEM	89.1	57.3	57.4	45.8	33.8	16.8	4.7
(S4)	SIM	116.7	54.7	83.3	43.5	13.2	12.2	5.3
	SWM	120.0	226.8	94.5	114.6	*12.0*	*27.6*	82.0
	FIM/NEM	109.8	98.5	81.1	72.9	*10.1*	*nd*	8.0
AS3	NEM	104.9	56.6	66.9	46.8	5.2	12.2	4.9
(S7)	SIM	93.0	57.6	71.9	46.3	9.2	10.6	5.0
	SWM	122.5	119.1	83.1	52.7	*10.6*	*13.8*	25.5
	FIM/NEM	*81.9*	79.8	65.2	63.9	*14.7*	*nd*	7.9
AS4	NEM	48.9	53.3	47.4	44.1	12.8	4.5	6.4
(S15)	SIM	54.0	32.0	47.6	32.6	nd	2.7	4.0
	SWM	117.6	120.3	71.0	67.4	*4.6*	*5.4*	12.2
	FIM/NEM	33.3	54.7	40.1	41.7	*2.5*	*nd*	9.8

Exceptions are given in italics where data from TN050 (SWM) and TN054 (NEM) have been substituted. Along with the station identifier defined for this report, the JGOFS site designation is provided in parenthesis. Descriptions of the methods used to obtain these in situ observations can be found on the U.S. JGOFS website (http://usjgofs.whoi.edu). Additional detail and analyses of the primary productivity (Barber et al., 2001) and the zooplankton (Smith et al., 1998a; Wishner et al., 1998; Roman et al., 2000) data sets can be consulted in the noted literature.

extrapolated to the trap depth, otherwise the extrapolation depth is 800 m (Table 3).

2.5. Definitions of season, region and terminology

Four months were chosen (Jan, Apr, Aug, Oct) to represent the high points of the monsoon and intermonsoon periods that dominate the northern IO and provide for the development of a seasonal description of the basin's biogeochemical variability. Furthermore, despite their northern bias, the monsoon (NEM/SWM) and intermonsoon (SIM/FIM = spring/fall intermonsoon) period descriptors are uniformly applied over the entire basin in order to identify consistently the seasonality of the variability and specific features that are discussed. We have also defined four basin sub-regions for our study, namely: (1) the Arabian Sea (west of 78 °E, north of 4 °N); (2) the Bay of Bengal (east of 78 °E, north of 4 °N); (3) the Equatorial band (±4°); and (4) the STIO (south of 4 °S). The boundaries for these four sub-regions are depicted in Fig. 1. Throughout this text, usage of the following terms is applied as follows. PP, nitrate, PON, and zooplankton biomass are always reported as areal values that have been vertically integrated. The term

Ekman pumping denotes upwelling into the surface layer unless specifically noted otherwise. To illustrate phytoplankton speciation shifts in the model, we define the ratio $P_R = P_S/(P_S + P_L)$. For P_R above 0.5 the picoplankton (P_S) dominate phytoplankton biomass, and for P_R below 0.5 netplankton (P_L) dominate. Where production or other diagnostics are given in carbon units the Redfield C/N ratio of 6.625 is used.

3. Results

3.1. Seasonal spatial distributions of modeled surface Chla compared to SeaWiFS climatology

3.1.1. The northeast monsoon (January)

In the Arabian Sea during the NEM, surface Chla typically exceeds 0.5 mg/m³ north of 15 °N (Fig. 2A). West of 65 °E, similarly elevated Chla extends to 10 °N. Overall, elevated Chla is present over the entire northern and western Arabian Sea, with oligotrophic conditions constrained to a wedge-shaped region in the southeast. Modeled Chla exhibits a similar distribution pattern, with oligotrophic conditions in the southeast and higher concentrations to the north and west (Fig. 3A). The

Table 3
Observed and model-predicted annual organic matter flux (mgN/m^2/d) at three sites in the Arabian Sea (AS2–AS4) and three sites in the Bay of Bengal (BB1–BB3)

Site	Trap depth (m)	Observed (annual mean)	Modeled rate of export flux		
			Annual mean	Monthly min	Monthly max
AS1	800		0.98	0.64	1.31
AS2 (MS3)	858	2.8	2.20	0.52	7.18
AS3 (MS4)	821	1.4	1.59	0.52	5.67
AS4 (MS5)	800	0.9	1.01	0.26	4.11
AS5	800		1.58	0.37	3.89
BB1 (NBBT)	809	1.5	0.55	0.39	0.76
BB2 (CBBT)	906	1.2	0.74	0.28	1.40
BB3 (SBBT)	1040	1.2	0.83	0.47	1.37
EQ1	800		0.51	0.24	1.42
EQ2	800		0.49	0.20	1.32
ST1	800		0.64	0.41	0.93
ST2	800		0.41	0.24	0.55

The coordinates for these six sites are listed in Table 1. The Arabian Sea observations were taken from Table 3 of Honjo et al. (1999). The Bay of Bengal observations were taken from Table 1 of Ittekkot et al. (1991). For AS1, AS5, EQ1, EQ2, ST1 and ST2 sites in the column 3, there are currently no available observations.
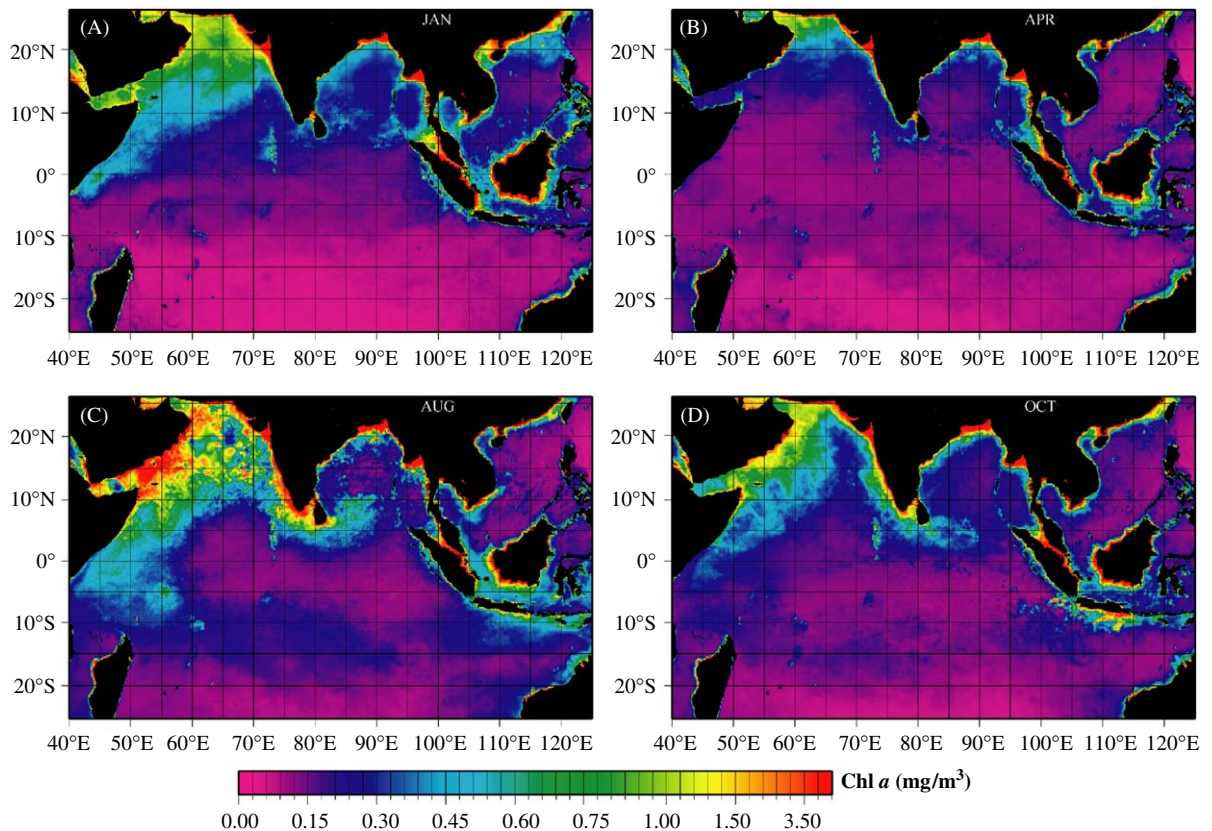
Fig. 2. Seasonal climatology of SeaWiFS chlorophyll (Jan, Apr, Aug, Oct). The climatology was created using monthly Level 3 Standard Mapped Image data from September 1997 through January 2002, which were obtained from the Goddard DAAC (http://daac.gsfc.nasa.gov/).
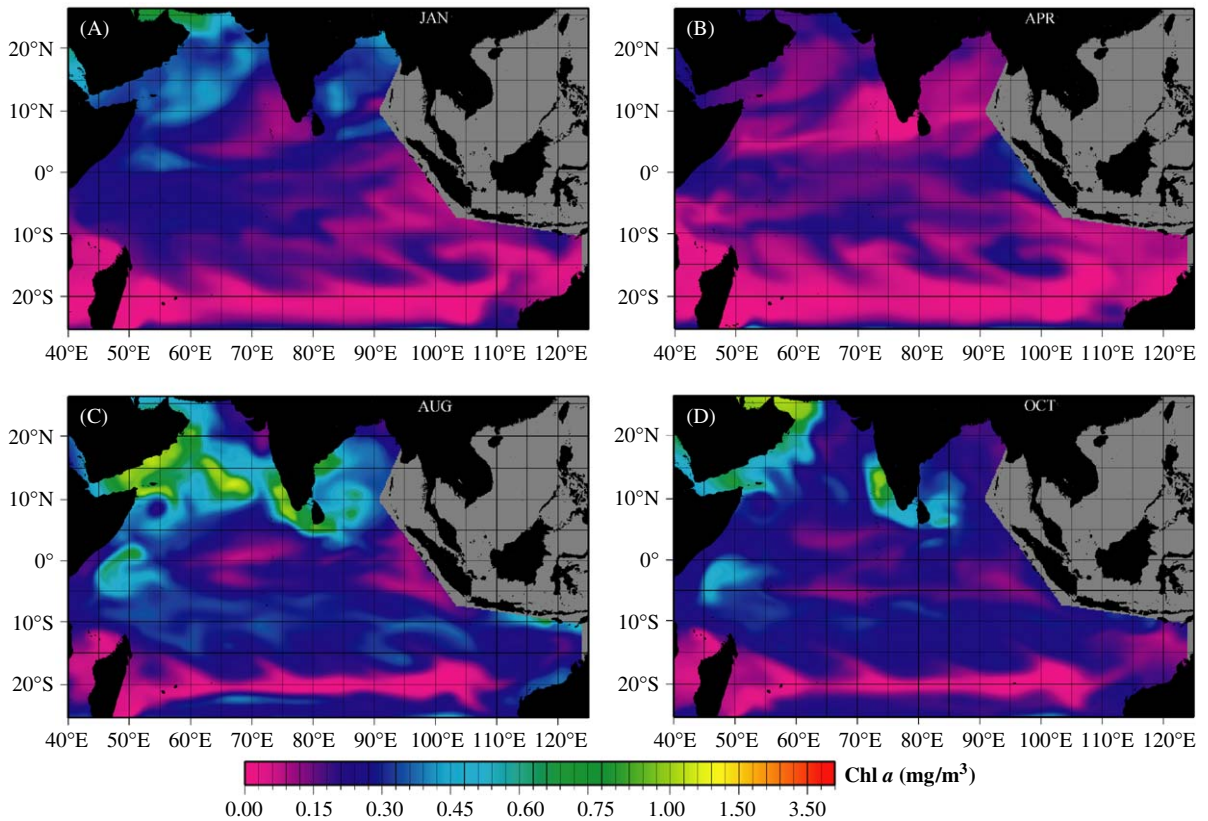
Modeled Chlorophyll *a*: 20m

Fig. 3. Seasonal surface Chl*a* (Jan, Apr, Aug, Oct) from the model solution.

wedge-like pattern of the lowest concentrations and the position of the transitional gradient between the two regions are also reproduced. However, the magnitude of modeled Chl*a* in the phytoplankton bloom region is generally lower than that observed by SeaWiFS, especially north of 15 °N, where Chl*a* never exceeds 0.5 mg/m^3 in the solution. These phytoplankton blooms are supported by nutrients entrained via convective mixing induced by the cool, dry northeasterly winds that characterize the NEM.

In the northern and western Bay of Bengal, the cool, dry air of the NEM also leads to elevated Chl*a* (~0.4 mg/m^3) that is comparable to the highest observed offshore concentrations north of 10 °N (Fig. 2A). In the model, Chl*a* along the eastern coast of India is somewhat lower (~0.3 mg/m^3), while offshore values are consistent with the observations (Fig. 3A). Along the southern portion of the Bay of Bengal between 5 °N and 10 °N, two distinct features with similar Chl*a* (~0.4 mg/m^3) are observed, one directly east of Sri Lanka and the other to the west of the northern tip of Sumatra

(Fig. 2A). Both are associated with persistent Ekman pumping and both have counterparts in the model that are more extensive spatially, though the eastern feature is shifted to the north in accordance with the NCEP wind-curl distribution (Fig. 3A).

In the equatorial band west of 47 °E observed Chl*a* reaches 0.8 mg/m^3, while between 47 °E and 54 °E concentrations of 0.3–0.4 mg/m^3 appear to the north (Fig. 2A). Over the rest of the equatorial region, Chl*a* does not exceed 0.2 mg/m^3 and a persistent meridional gradient is apparent, with southern concentrations as low as 0.1 mg/m^3. While the maximum off the coast of Somalia does not appear, modeled Chl*a* does exhibit the offshore feature north of the equator in the west (Fig. 3A). The cross-equatorial Chl*a* gradient is also apparent in the solution. In the STIO, Chl*a* concentrations are uniformly low (0.1 mg/m^3 or less, Fig. 2A). Modeled concentrations are slightly higher, but the region's oligotrophic character is captured (Fig. 3A). Both observed and modeled

Chl$a$ decline to concentrations below 0.15 mg/m^3 south of 10 °S.

3.1.2. The spring intermonsoon (April)

In the northern IO, the SIM is a period of shallow mixed layers resulting from weak wind stirring and increased solar heating. This results in oligotrophic conditions and reduced Chl$a$ (Fig. 2B). In both the Arabian Sea and the Bay of Bengal, elevated Chl$a$ only appears relatively close to the northern coastal shelves. The central and southern portions of the Bay exhibit oligotrophic conditions, with concentrations of Chl$a$ generally between 0.1 and 0.2 mg/m^3, while in the corresponding areas of the Arabian Sea concentrations are slightly higher, ranging up to 0.3 mg/m^3 (Fig. 2B). The model captures the oligotrophic nature of both regions (Fig. 3B). The one significant difference between the model and the observations occurs in the northernmost portion of the Arabian Sea where elevated Chl$a$ (>0.7 mg/m^3) is observed.

Chl$a$ along the equatorial band is uniformly low away from the land boundaries (Fig. 2B). Chl$a$ in the model exhibits similar homogeneity, though with somewhat higher concentrations (Fig. 3B). Adjacent to both the western and eastern land boundaries in the model, elevated Chl$a$ (>0.2 mg/m^3) extends farther offshore than observed due to the smearing of coastal upwelling features. Off the coast of Sumatra the difference between the observed and modeled distribution is most pronounced. In the model, a low magnitude Chl$a$ feature extends westward of 90 °E, whereas in the SeaWiFS climatology similar levels of Chl$a$ are only apparent in close proximity to Sumatra and do not extend past 97 °E (Figs. 2B and 3B).

In the STIO, observed Chl$a$ increases slightly from the NEM and the most oligotrophic conditions no longer extend north of 15 °S (Fig. 2B). Overall, modeled Chl$a$ is consistent with the observations, with concentrations of ∼0.2 mg/m^3 centered along 10 °S and the most oligotrophic areas manifesting to the south (Fig. 3B). The model's success at simulating this region's surface Chl$a$ during the SIM underscores the discrepancies that appear in the NEM, as modeled Chl$a$ decreases between the two periods while the observations display the opposite trend.

3.1.3. The southwest monsoon (August)

During the SWM, phytoplankton blooms (Chl$a > 1.0$ mg/m^3) extend from the coasts of Somalia and the Arabian Peninsula well into the central Arabian Sea (Fig. 2C). South of 15 °N, similarly elevated concentrations are also observed along the entire west coast of India. These blooms are represented in the model (Fig. 3C). The model also reproduces the offshore blooms, although their magnitude is generally lower than observed. The nutrients that fuel these blooms are transported into the euphotic zone by coastal upwelling, offshore advection, Ekman pumping and wind-induced mixed-layer deepening, all of which are driven by the Somali Jet. In addition, the phytoplankton distribution along the northern Somali coast indicates that the center of the Great Whirl, which appears as a circular, low Chl$a$ feature in the solution, is consistent with its position (8 °N, 53 °E) in the SeaWiFS climatology (Figs. 2C and 3C).

In the Bay of Bengal, elevated chlorophyll concentrations ranging from 0.6 to 0.8 mg/m^3 occur east of Sri Lanka during this period between 5 °N and 10 °N around 85 °E (Fig. 2C). South and east of this feature, lower concentrations (∼0.4 mg/m^3) appear that coincide with the path of the northeast branch of the SMC as it wraps around the cyclonic Sri Lanka Dome. This distribution of Chl$a$ is the region's most prominent biological feature (Fig. 2). Modeled Chl$a$ shows excellent spatial correspondence with this feature's observed pattern (Fig. 3C). North of 10 °N, Chl$a$ in the model shows offshore values approaching 0.4 mg/m^3 whereas the observed concentrations in the SeaWiFS climatology do not exceed 0.15 mg/m^3. This discrepancy is attributable to the lack of riverine input in the model configuration and will be discussed in more detail in Section 3.2.2.

The equatorial band is oligotrophic with two exceptions. Westward of 57 °E observed Chl$a$ exceeds 0.3 mg/m^3, with concentrations reaching 0.5–0.6 mg/m^3 between 45 °E and 50 °E (Fig. 2C). Between 75 °E and 90 °E, south of India, observed Chl$a$ ranges from 0.4 to 0.5 mg/m^3. Both features appear in the model. The former is the biological signature of the Southern Gyre, while the latter marks the path of the SMC as it exits the Arabian Sea (Fig. 3C). In the STIO, curl-driven upwelling reaches its annual peak during the SWM, which initiates the region's austral winter phytoplankton bloom. Observed Chl$a$ is at least 0.2 mg/m^3 between 5 °S and 15 °S and elevated concentrations extend farther south between 70 °E and 85 °E (Fig. 2C). Both the higher Chl$a$ concentrations in the west with decreasing values south of 15 °S, and the

contrast in Chl*a* concentration between the northern IO and the STIO are reproduced by the model (Fig. 3C). However, Chl*a* is higher than observed, which we attribute to the lack of an ITF in this model configuration (i.e. the nutricline is too shallow).

3.1.4. The fall intermonsoon (October)

As the monsoon winds relax going into the FIM, the basin's SWM-period phytoplankton blooms dissipate. Modeled Chl*a* agrees well with the SeaWiFS climatology, as in both distributions the two most prominent features appear along the Arabian Peninsula and the southwest coast of India (Figs. 2D and 3D). In the Bay of Bengal, the elevated chlorophyll values east of Sri Lanka now extend to only 7 °N and the maximum concentration has decreased to ~0.5 mg/m^3 (Fig. 2D). This is a response to reductions in both local Ekman pumping and advection by the SMC and is accurately reproduced by the model (Fig. 3D).

As during the SWM, the two most prominent biological features in the equatorial band are along the Somali coast and south of India (Fig. 2D). Modeled Chl*a* along the coast of Somalia north of the equator is consistent with the observations, while south of the equator it is up to twice as high (Figs. 2D and 3D). This indicates that Southern Gyre upwelling is too intense at this time in the model, possibly due to errors in the wind forcing. South of India, elevated Chl*a* does not extend as far south in the model as in the observations (Fig. 3D), suggesting that the SMC in the model is not energetic enough. This could be due to the lack of freshwater injections in the Bay of Bengal that tend to reduce the depth of the upper model layer, thus intensifying surface currents. In the STIO, modeled Chl*a* is generally higher than observed, as the reestablishment of oligotrophic conditions occurs later (Figs. 2D and 3D). Again, this probably reflects a too shallow nitracline that results from the lack of an ITF in the model.

3.2. Seasonal biogeochemical response to regional forcing and inter-regional connections

3.2.1. Monsoon-driven biogeochemical properties in the Arabian Sea

At AS1, the most notable difference between modeled and surface Chl*a* in the SeaWiFS climatological time series is the magnitude of the phytoplankton bloom during the NEM/SIM transition,

which is much less pronounced in the model (Fig. 4A). Comparison of the solution to the JGOFS observations reveals that PP, PON and zooplankton biomass show excellent agreement during the NEM but that the model ecosystem is significantly less productive during the SIM. A somewhat lower nutrient load in the model may be the cause of the latter (Fig. 5A). The water-column distribution of phytoplankton biomass during the SIM also exhibits significant differences as the observations reveal a shallow DCM (40–50 m) that has achieved its annual concentration maximum (see Fig. 8 in Gundersen et al., 1998), whereas the model DCM is at its deepest (70–85 m) and has reached its annual minimum (Fig. 6A). In the model the low subsurface values of Chl*a* (0.6–0.7 mg/m^3) are collocated with the 0.5 μM nitrate isopleth and persist into May despite the shoaling of the mixed layer, which further indicates that not enough nutrients are present at this time in the solution. The modeled DCM exhibits a speciation shift toward larger phytoplankton (Fig. 6A) that is consistent with the observations (Latasa and Bidigare, 1998).

From the mid-SWM through the FIM, the model (DCM) resides at 60–70 m and intensifies moderately (Fig. 6A). These attributes show good correspondence with the observed DCM. The surface Chl*a* time series during this time also correspond well with the SeaWiFS climatology (Fig. 4A). Further, PON and zooplankton biomass from these two periods are consistent with the JGOFS observations, as is PP during the SWM (Table 2). Interestingly, while the model indicates a definitive speciation shift toward netplankton associated with the peak in DCM magnitude ($P_R < 0.35$), there is only a slight corresponding increase in particle flux and rates of organic matter export remain below 2 mgN/m^2/d throughout the year (Figs. 4A and 6A).

At AS2 and AS3, the simulated phytoplankton bloom during the NEM/SIM transition is also less prominent, though the difference between surface Chl*a* in the model and in the SeaWiFS climatology is not as severe as at AS1 (Figs. 7A–C). Rates of PP at AS2 and AS3 during the NEM and SIM are 36–53% lower than observed; particulate matter and zooplankton biomass are similarly underrepresented (Table 2). Furthermore, the secondary particle flux maxima at these two sites do not manifest in the solution (Figs. 7A, B). For all of these metrics the clearest differences between the model and the observations during the NEM and
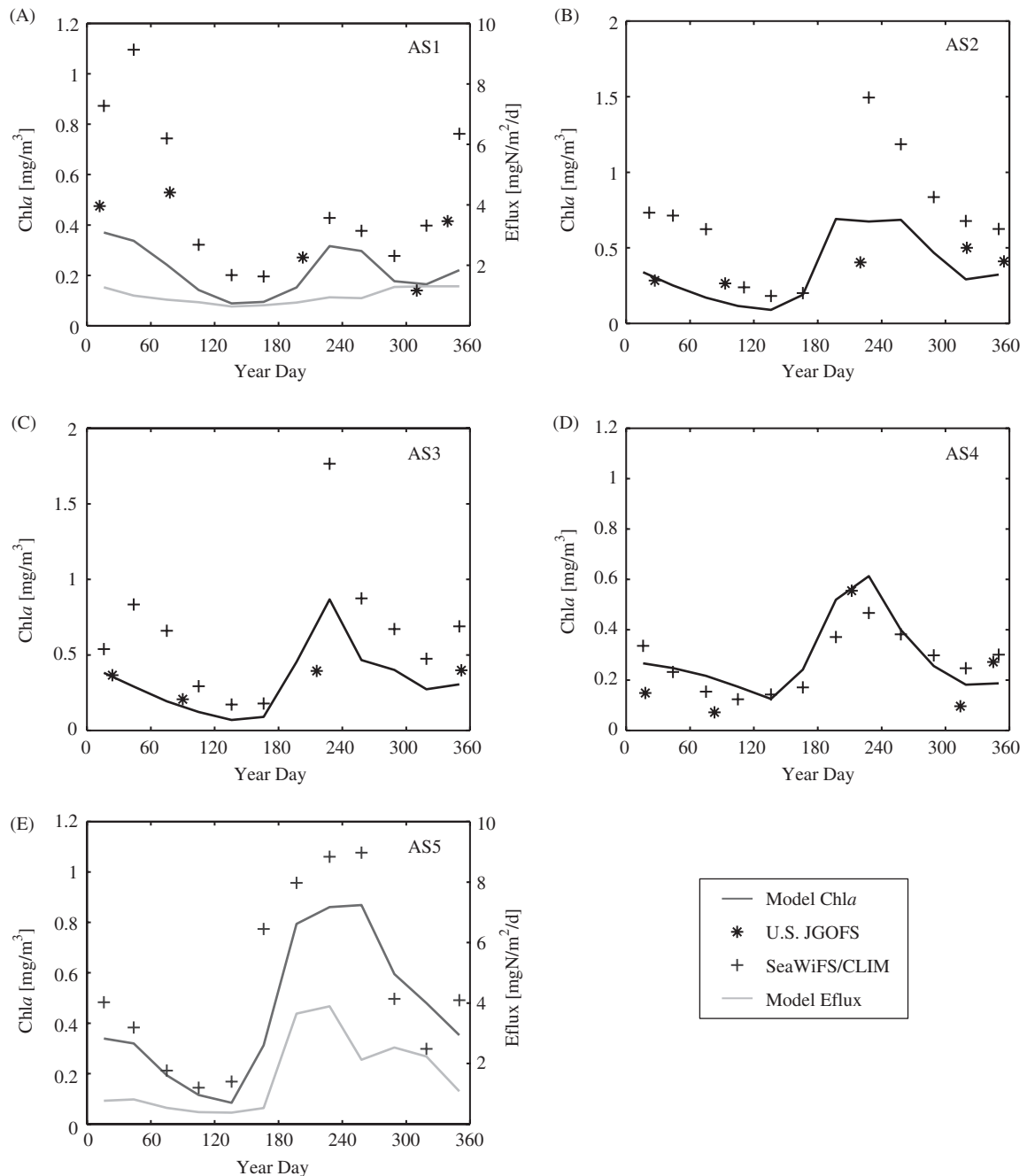
Fig. 4. Surface Chl*a* (mg/m^3) from the model solution (dark line) compared with the SeaWiFS climatology (+) and the US JGOFS in situ observations (●) at five sites in the Arabian Sea (AS1–AS5). Note that no JGOFS measurements were available for AS5 (5E). Model organic matter flux at AS1 and AS5 are also shown (light line) on 5A and 5E. These time series have been extrapolated to 800 m. The coordinates for the five sites are listed in Table 1.

SIM occur at AS2. The corresponding nutrient loads at AS2 are also consistently lower than indicated in the NODC climatology, whereas model values at AS3 show better correspondence

(Figs. 5B, C). At both sites, the observed 0.5 μM nitrate isopleth shoals to the surface during the NEM, whereas in the model it remains below 40 m (Figs. 6B, C). Modeled Chl*a* in the DCM is lower at
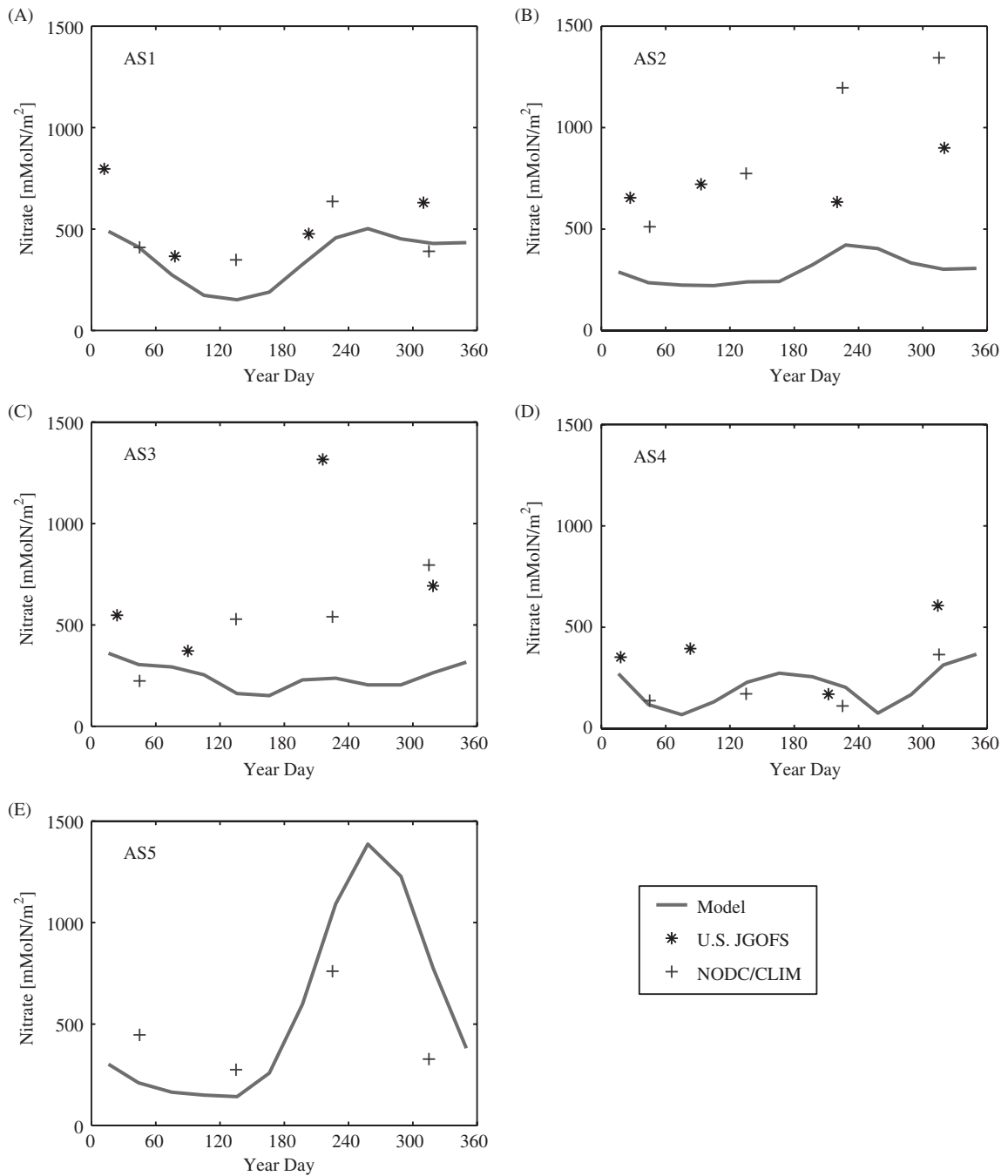
Fig. 5. Vertically integrated nitrate (mmolN/m^2) from the model solution (solid line) compared with JGOFS in situ measurements (●) from process cruises TN043, TN045, TN049 and TN053, respectively (Table 2 provides seasonal definitions for these cruise designations). The crosses (+) are vertically integrated seasonal profiles from the NODC World Ocean Atlas (Conkright et al., 1998). The integration is carried out over the upper 100 m. The coordinates for the five sites are listed in Table 1.

both sites when the modest NEM-period surface blooms occur while maximal subsurface concentrations appear during the SIM between 70 and 90 m

(Figs. 6B, C). While the temporal evolution at both locations is similar, the observed DCM depths do not exceed 50 m, Chla values are notably higher
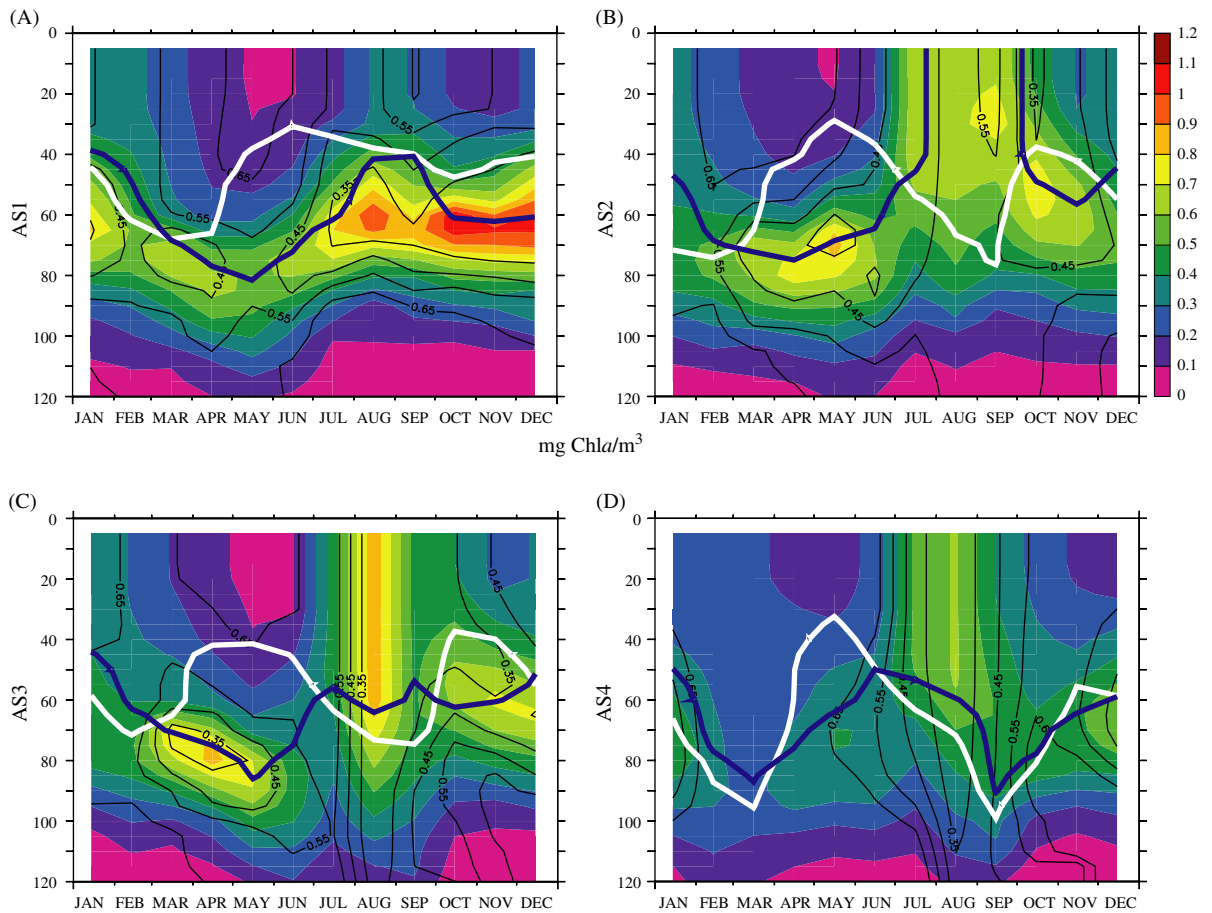
Fig. 6. Time series of Chl$a(z)$ over the upper 120 m at the four model extraction sites (AS1–AS4) that correspond to standard U.S. JGOFS sampling locations (see Table 1). The superimposed contours are of P_R that indicates phytoplankton speciation shifts (see definition in Section 2.5). The blue line shows the temporal evolution of the 0.5 μM NO$_3$ isopleth. The white line shows the temporal evolution of mixed-layer depth.

(see Fig. 9 in Gundersen et al., 1998), and the model indicates a subsurface phytoplankton speciation shift that is not apparent in the HPLC data (Latasa and Bidigare, 1998).

Phytoplankton blooms develop in the model at AS2 and AS3 during the SWM (Figs. 4B, C). The peak concentrations in the SeaWiFS climatology (from August) are 100–120% greater than the corresponding Chl$a$ values from the model and are notably higher than those measured during the JGOFS surveys, which are even lower than the model concentrations. Unfortunately, the in situ measurements are from mid-July when SeaWiFS observations are unavailable so a direct comparison to the satellite-based climatology cannot be performed. At AS2, surface chlorophyll concentrations of 0.6–0.7 mg/m^3 persist for three months in the

solution; concentrations at AS3 are lower except during the August maximum (Figs. 4B, C). The difference in the character of these blooms in the model is related to the vertical distribution of nutrients. At AS2, the 0.5 μM nitrate isopleth extends to the surface from July through September, which is indicative of coastally upwelled, high-nutrient waters advecting to this location in the model (Fig. 6B). On the other hand, at AS3 this isopleth remains below 55 m (Fig. 6C), which is contrary to the observations that indicate surface nitrate concentrations exceeding 0.5 μM at both sites (Gundersen et al., 1998). The solution indicates increased netplankton abundance in August over at least the upper 50 m at AS2 and AS3 (Figs. 6B, C), which is consistent with the HPLC analysis of Latasa and Bidigare (1998). At AS2, two of the
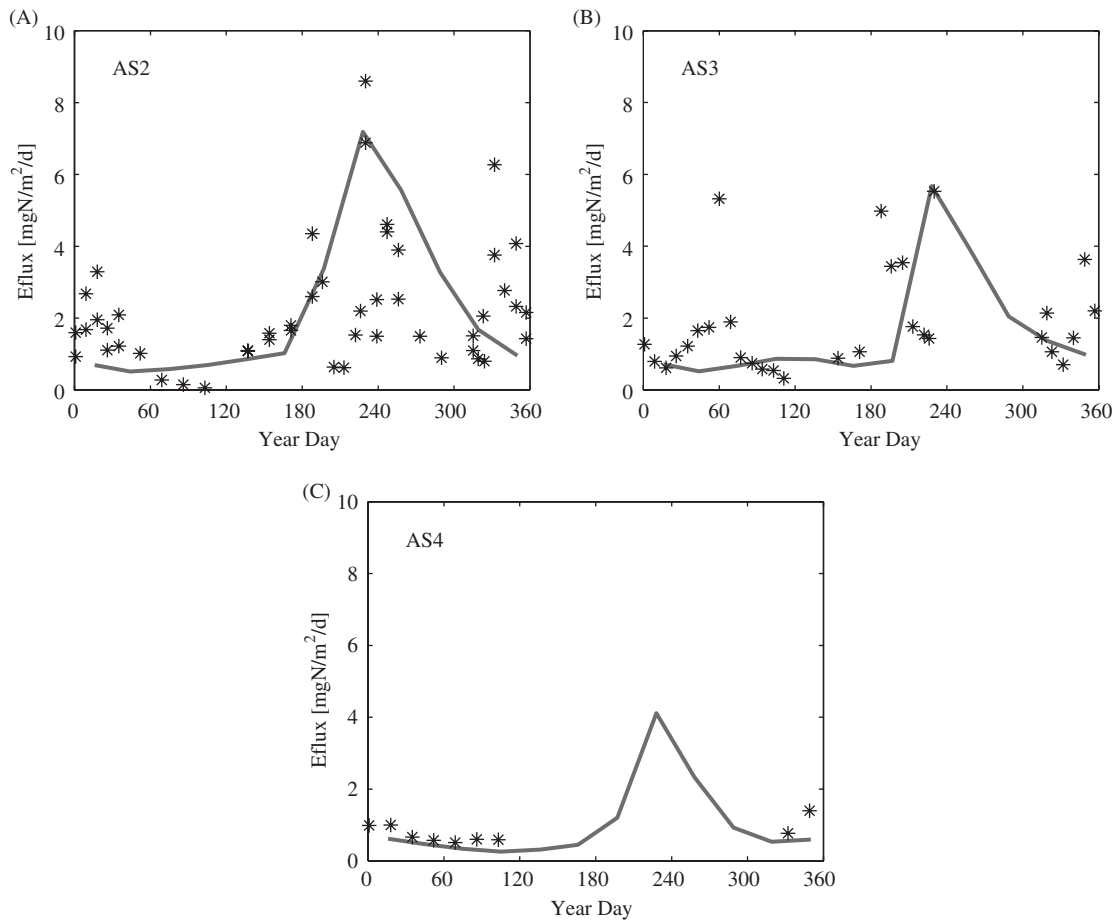
Fig. 7. Organic matter flux (mgN/m^2/d) from the model solution (solid line) compared with JGOFS sediment trap data (●) from traps M3 (AS2), M4 (AS3), M5 (AS4). Model export fluxes have been extrapolated to the trap depth (873, 814 and 800 m, respectively) using the Martin curve. The coordinates for the three sites are listed in Table 1.

highest model-data differences in PP (89%) and zooplankton biomass (198%) occur and while PP at AS3 is nearly identical to the observed rate, zooplankton abundance (85%) and PON (37%) are both somewhat higher (Table 2). SWM-period export flux in the model is consistent with the sediment trap measurements at both sites (Figs. 7A, B).

At AS4, the surface Chla comparison between the simulation, the JGOFS data and the SeaWiFS climatology is excellent, as is the comparison between modeled nitrate and the NODC climatology (Figs. 4D and 5D). The seasonal comparison between the model and the JGOFS observations of PP, PON and zooplankton abundance is very good (Table 2), with PP and zooplankton biomass during the FIM showing the most notable differences. The SWM surface bloom that peaks in August evolves

into a DCM as the mixed layer deepens going into the FIM (Fig. 6D). This model DCM intensifies as the NEM progresses and both its first appearance and subsequent evolution through the NEM correspond well with the observations. However, it dissipates during the SIM whereas the observed DCM intensifies and remains well defined at ∼75 m. This mismatch between modeled and observed DCM evolution is due to the model mixed-layer deepening beyond 90 m in March (Fig. 6D), while the SIM mixed layer reported by Gundersen et al. (1998) shoals above 25 m. Both the HPLC analysis and the model indicate that the SIM is dominated by picoplankton. During the SWM phytoplankton bloom, a shift toward netplankton manifests in the model (Fig. 6D). While a shift toward diatoms is not indicated by the HPLC data, Latasa and Bidigare (1998) do report a speciation shift to an

intermediate size class composed largely of dino-flagellates. Model export flux shows excellent correspondence to the available sediment trap data, though unfortunately there are no observations during the SWM so the summertime maxima indicated by the model cannot be verified (Fig. 7C).

Observations of zooplankton biomass and grazing rates at AS4 demonstrate that mesozooplankton are not prominent and that a regenerative system characterized by a close coupling between phytoplankton growth and microzooplankton grazing manifests during both monsoon periods (Landry et al., 1998; Smith et al., 1998a). Nearer to shore this trophic coupling breaks down and mesozooplankton biomass increases (Banse, 1994; Wishner et al., 1998; Stelfox et al., 1999). This spatial characterization is observed throughout the year and is especially pronounced during the monsoons. During the NEM, this spatial gradient does not manifest in the solution. During the SWM, the model exhibits a definitive shoreward increase in zooplankton biomass with values at AS2 and AS3 that are ~7x and ~2x greater (respectively) than those at AS4 (Table 2). Additionally, microzooplankton account for ~90% of zooplankton biomass at AS4 during the SWM, whereas at AS3 and AS2 they contribute ~70% and 40%, respectively.

3.2.2. Biogeochemical variability in the Bay of Bengal

Modeled Chl$a$ at BB1 and BB2 indicates semiannual phytoplankton blooms at these two sites, with the maxima occurring during the monsoons (Figs. 8A, C). Though of lower magnitude, this semiannual character is similar to the bloom dynamics of the Arabian Sea and results from similar monsoonal forcing. However, this semiannual cycle is not present in the SeaWiFS climatology (Figs. 8A, C) and as noted earlier Chl$a$ concentration north of $10\,°N$ is markedly higher in the model (Section 3.1.3). Instead of the semiannual cycle that appears in the model, observed Chl$a$ at BB1 is essentially constant while only the NEM bloom is observed at BB2. Nitrate at BB1 shows good correspondence during the SWM and the annual mean shows good correspondence to the NODC data, though the temporal patterns differ (Fig. 8B). At BB2, modeled nitrate is consistent with the climatology (Fig. 8D).

Modeled export flux at BB1 has no distinct seasonal cycle and is maximal during the FIM (Fig. 8A). At BB2, a prominent annual cycle is apparent with the maximum flux again occurring during the FIM (Fig. 8C). Ramaswamy and Nair (1994) collected five years of sediment trap observations at three locations; export maxima during both the monsoons were observed at the two northern traps (BB1 and BB2). Modeled particle flux at these two locations is therefore inconsistent with the observed variability. The discrepancies in the evolution of surface Chl$a$ and particle flux at these two sites are likely due to not including riverine inputs and their associated terrigenous materials in the model. Indeed, a recent study reports that lithogenic material at these two sites annually contributes 30–40% to total particulate flux (Unger et al., 2003). Moreover, during the SWM the freshwater river plume has been observed to extend southward to ca. $10\,°N$. Recent analyses suggest that this freshwater cap prevents surface nitrate enrichment of the Bay of Bengal by monsoon winds and therefore inhibits the development of summertime phytoplankton blooms north of $10\,°N$ (Kumar et al., 2002; Madhupratap et al., 2003).

On the other hand, modeled Chl$a$ at BB3 corresponds well to the SeaWiFS climatology, especially from the NEM through the initial mid-SWM phytoplankton bloom (Fig. 8E). The magnitude of modeled nitrate agrees with the NODC climatology, but the temporal trend is reversed (Fig. 8F). The temporal evolution of modeled export flux (Fig. 8E) shows good qualitative agreement with the observations. Both time series show an annual maximum appearing mid-SWM through FIM (Ramaswamy and Nair, 1994) and modeled annual flux is within 50% of the observed rate (Table 3).

3.2.3. Biogeochemical response to the Somali Current during the SWM

During its northward flowing phase, the Somali Current adopts the character of a western boundary current and includes two anticyclonic gyres that appear along the Somali Coast. These are the Great Whirl and the Southern Gyre, and both intensify as the SWM progresses. In May, the Great Whirl has already formed a closed circulation in the model between $7\,°N$ and $8\,°N$ while the genesis of the Southern Gyre appears as an offshore deflection between the equator and $2\,°N$ (Fig. 9A). By June the model shows that the Great Whirl has intensified while the offshore deflection near the equator has evolved into a current meander. This meander splits into an eastward branch and a southwestward
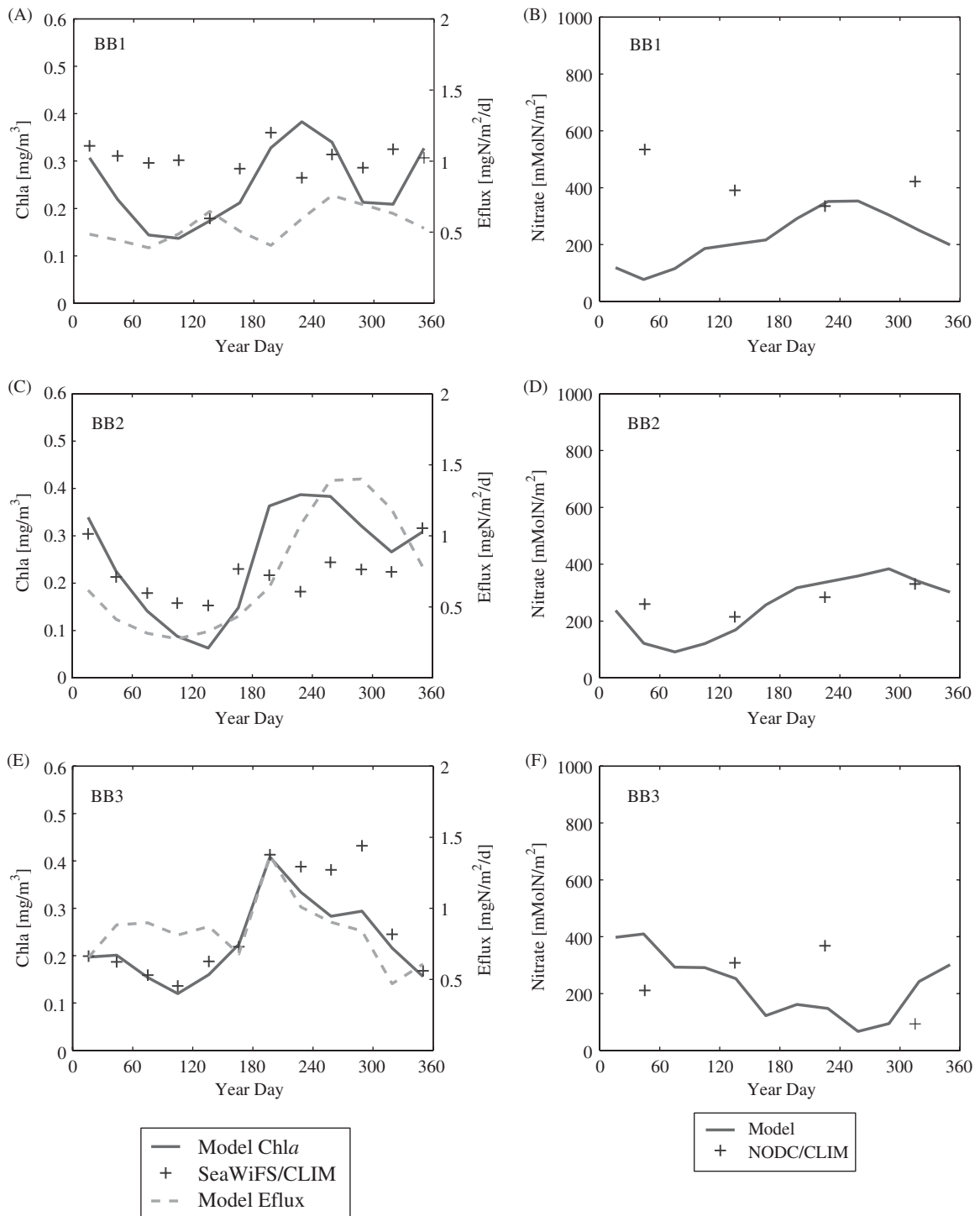
Fig. 8. (A) Surface Chl*a* (mg/m³) from the model solution (solid line), SeaWiFS Chl*a* climatology (+), and model organic matter flux in mgN/m²/d (dashed line) at BB1. (B) Vertically integrated nitrate from the model (solid line) compared with the NODC climatology (+) at BB1. The integration is carried out over the upper 100 m. (C) Same as 8 (A) but for BB2. (D) Same as 8 (B) but for BB2. (E) Same as 8 (A) but for BB3. (F) Same as 8 (B) but for BB3. The coordinates for the three sites are listed in Table 1.
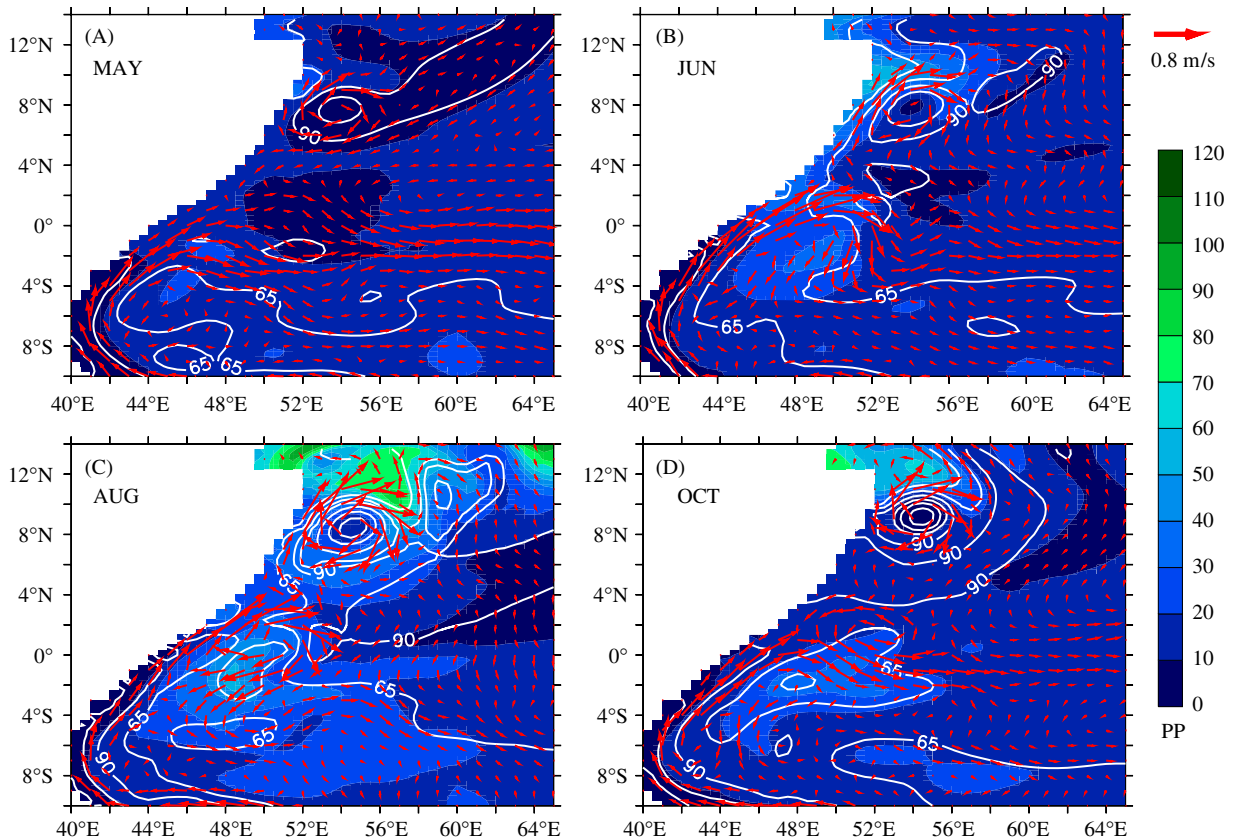
Fig. 9. Vertically integrated primary production (PP, in mmolC/m^2/d), nitracline depth (superimposed contours) and horizontal current vectors associated with the Somali Current over the course of the SWM. The four months used to illustrate this progression are (A) May; (B) June; (C) August; and (D) October. The nitracline is defined as the depth at which nitrate concentration reaches 1.4 μM. The current vectors are from 40 m.

branch that rejoins the northward flowing coastal current at ∼4 °S, forming the Southern Gyre (Fig. 9B). At this time, the modeled nitracline is everywhere above 65 m along the coast and is shallowest in two wedges that appear northwest of each gyre. Both features exhibit a biological response, which the model indicates is stronger around the Great Whirl (Fig. 9B). The location and character of the biogeochemical fields that accompany the two gyres, as well as the relative intensity of their biological responses, are all consistent with the 1979 INDEX cruise observations of these two features (Smith and Codispoti, 1980).

In the model, the Great Whirl's location and the intensity of its surrounding current field persist from July through September (Fig. 9C). Convergence within the Great Whirl drives the nitracline below 120 m, which creates a core of low biological activity that spatially coincides with the low Chl*a* feature in the SeaWiFS climatology (Figs. 2C and 3C).

Indeed, the Chl*a* comparison at AS5 reveals that the model succeeds in reproducing both the seasonal variability and the magnitude of the summer bloom (Fig. 4E). The most productive waters in the model, with rates of 50–100 mmolC/m^2/d, are offshore and north of the Great Whirl while rates exceeding 30 mmol C/m^2/d surround the feature (Fig. 9C). The nutrient-rich coastal waters that have been dynamically upwelled, and subsequently entrained, by the Great Whirl's vigorous circulation fuel this elevated primary production. Veldhuis et al. (1997) report rates of primary production of 64–97 mmol C/m^2/d in the newly upwelled waters near shore and higher rates (up to 240 mmol C/m^2/d) in the more developed blooms around the Great Whirl's northern limb. Integrated nitrate is generally consistent with the NODC climatology, though nutrient loads in the model are somewhat higher during the SWM and FIM (Fig. 5E). While the SWM particle flux maximum at both AS2 and AS3 significantly

exceeds that at AS5 in the model, elevated export at AS5 persists through the FIM (Figs. 4E and 7A, B). This results in an annual flux of organic matter at AS5 is similar to that at AS3, which is the second highest over the entire basin (Table 3).

In contrast to the Great Whirl, the Southern Gyre moves slowly northward throughout the SWM in the model. During June it is centered at ~3 °S and the peak associated production rates (40–50 mmol C/m^2/d) lie within the upwelling wedge that appears along the Somali coast at 2 °N (Fig. 9B). Smith and Codispoti (1980) observed a production rate of 112 mmol C/m^2/d in this upwelling wedge during July of 1979. During August, the Southern Gyre's circulation in the model is centered north of the equator while the associated produc-

tion maximum (60 mmolC/m^2/d) and shallowest nitracline extend from the equator to 3 °S (Fig. 9C). The model extraction point EQ1 is situated on the eastern side of the Southern Gyre at this time. At EQ1, increasing Chla in the model associated with the Southern Gyre's evolution coincides with the SeaWiFS climatology, the highest rate of export flux in the model (outside of the Arabian Sea) is achieved and modeled nitrate is consistent with the NODC climatology (Figs. 10A, B and Table 3). Upwelling within the Southern Gyre before it reaches the equator is the primary nutrient source for this biological activity (Fig. 9C), though nutrients upwelled at ~2 °N and subsequently transported around the Southern Gyre also may contribute.
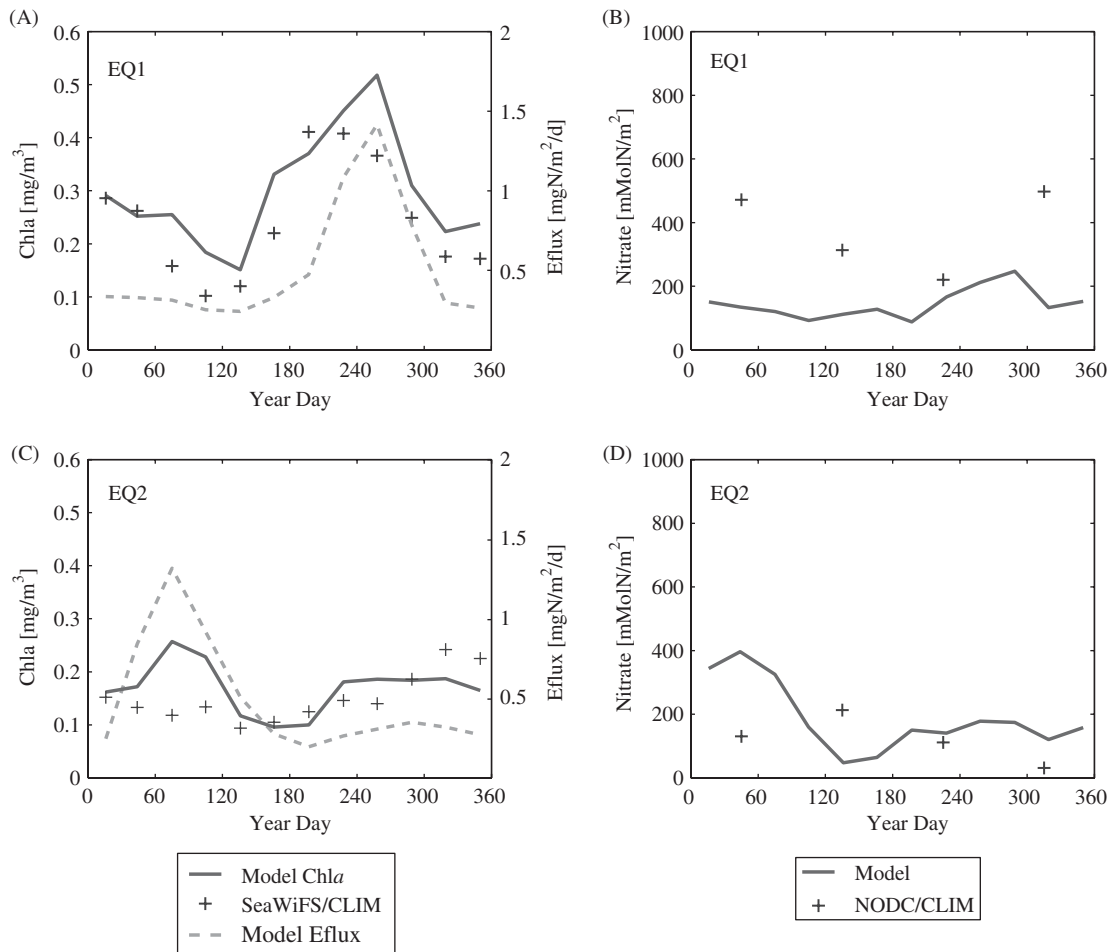

Fig. 10. (A) and (C) Surface Chla (mg/m^3) from the model solution (solid line) compared with the SeaWiFS climatology (+) at the two equatorial sites (EQ1 and EQ2). Model organic matter flux at the two sites is also shown (dashed line). (B) and (D) Vertically integrated nitrate from the model (solid line) compared with the NODC climatology (+) at the two equatorial sites (EQ1 and EQ2). The integration is carried out over the upper 100 m. The coordinates for the two sites are listed in Table 1.

As the monsoon winds dissipate in September–October, the model nitracline deepens south of the Great Whirl and production declines (Fig. 9D). However, its circulation remains coherent and elevated production of 40 mmolC/m^2/d still appears to the north. Additionally, both surface Chl$a$ and organic matter export remain elevated at AS5 (Fig. 4E). On the other hand, the Southern Gyre has completely dissipated by October and it can be seen that the equatorial westerlies have already triggered the fall Wyrtki Jet (Fig. 9D). Yet, model production rates of ~40 mmolC/m^2/d associated with the remnants of the shallow nitracline are still apparent south of the equator, and surface Chl$a$ and export flux at EQ1 remain elevated (Figs. 9D and 10A).

3.2.4. Biogeochemical response to Wyrtki Jet propagation

While the Southern Gyre dynamics that promote the ecosystem response at EQ1 are distinct from those at EQ2, it is nevertheless instructive to compare annual biogeochemical variability in the model at these two equatorial sites. At EQ1, peak export flux coincides with peak values of surface Chl$a$ that are consistent with the SeaWiFS climatology (Figs. 2C, 3C and 10A). At EQ2, Chl$a$ concentration peaks during the SIM in the model. These values are somewhat higher than those in the SeaWiFS climatology but are about 50% lower than peak concentrations at EQ1 (Figs. 10A, C). Despite the much weaker surface bloom, the SIM-period export flux maximum at EQ2 is similar in
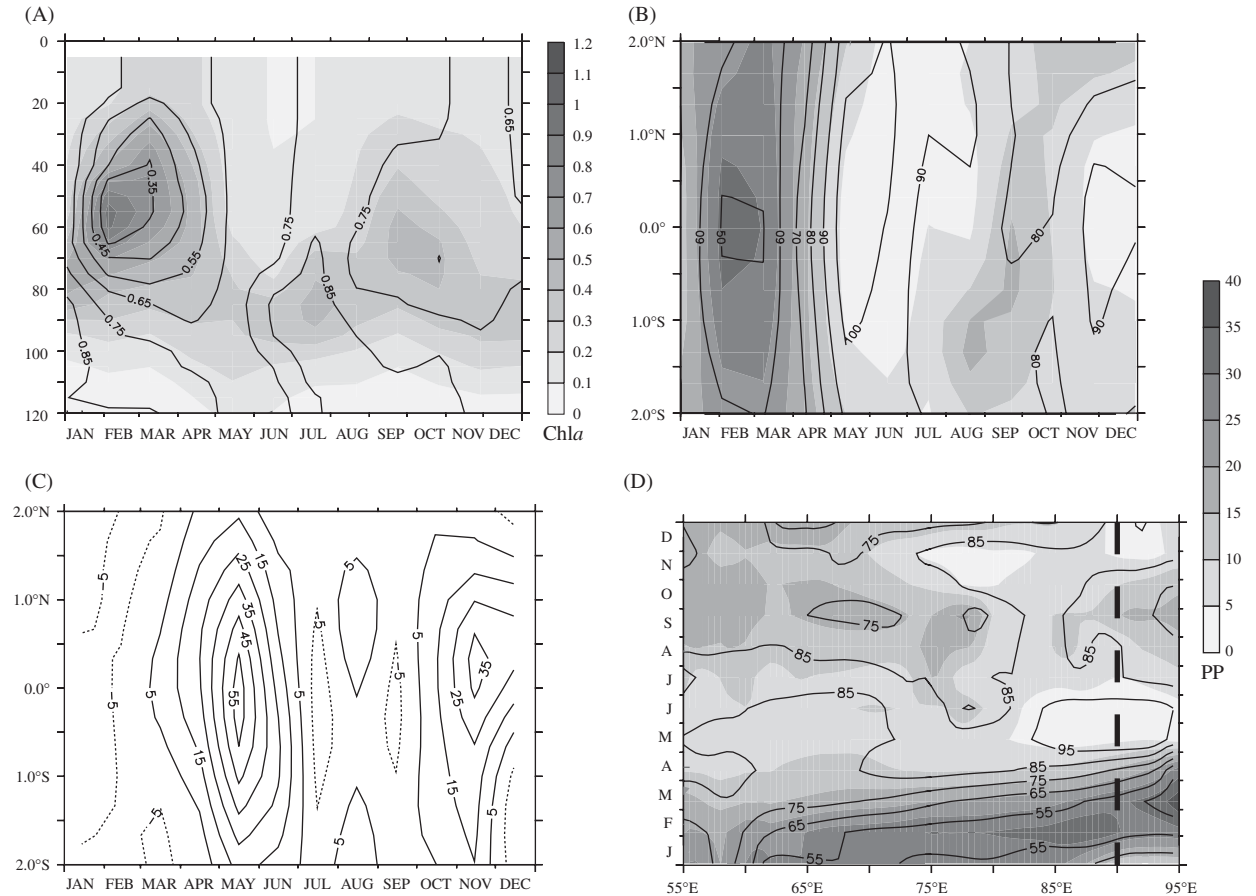

Fig. 11. (A) Time series of Chl$a(z)$ (mg/m^3) at EQ2 (90 °E). The superimposed contours are $P_R(z)$. (B) Meridional section of vertically integrated primary production (mmol C/m^2/d) along 90 °E. (C) Meridional section of zonal volume transport (m^2/s) along 90 °E. The lower integration limit (80 m) coincides with the base of the shear layer. (D) Vertically integrated primary production (mmol C/m^2/d) along the equator. The vertical dashed line indicates the location of extraction site EQ2. The superimposed contours on figures (B) and (D) are nitracline depth (m).

magnitude to the peak rate at EQ1 (Figs. 10A, C). This suggests that EQ2's biogenic matter must primarily originate at depth, and a notable DCM is indeed present between 50 and 60 m (Fig. 11A). The associated values of P_R (<0.35) denote a strong shift toward netplankton that is conducive to generating the noted export flux peak at EQ2. This DCM coincides with maximal cross-equatorial nitracline shoaling at 90 °E (Fig. 11B). While nitrate concentrations in the model are higher than observed during the SIM (Fig. 10D), the quarterly NODC climatology does indicate a doming in equatorial nitrate isopleths to ~60 m between 90 °E and 95 °E (data not shown) that is consistent with the model's nitracline behavior. Thus, despite its relatively weak surface expression, this biological response to a seasonally elevated nitracline appears to be likely. Further, the model suggests that an upward perturbation of the nitracline in the eastern IO during the SIM will trigger a notable biological response in surface waters.

The cross-equatorial shoaling of the model nitracline also coincides with the annual maximum in equatorial PP at 90 °E and the nitracline's subsequent precipitous deepening results in an order of magnitude reduction in PP by May (Fig. 11B). Another, less dramatic, nitracline shoaling/deepening cycle initiates during the late SWM. This semiannual deepening of the nitracline coincides with the Wyrtki Jet's arrival in the eastern IO, which is illustrated by the meridional section of zonal volume transport (Q_X) along 90 °E (Fig. 11C). In the model, the fall jet is weaker than its springtime counterpart, but both inhibit the ecosystem in the eastern equatorial IO by depressing the nitracline (Fig. 11B). The eastward progression of the spring jet is apparent in the temporal evolution of water column PP and nitracline depth across the equatorial IO (Fig. 11D). The arrival of the fall jet is similarly evident, although its biogeochemical impact is less pronounced.

Once the Wyrtki Jet reaches the Sumatra coast, its energy propagates poleward as coastal Kelvin waves and a portion of the northward propagating energy radiates across the Bay of Bengal as Rossby waves. Along 4.3 °N in the southern Bay of Bengal, a reduction in primary production of two months duration closely follows the equatorial impingement of both Wyrtki Jets (Fig. 12A). During the NEM, the reflected fall Wyrtki Jet dampens primary production in the southeastern Bay despite the prevailing Ekman pumping. During the early SWM,

the drop in production is more acute and it propagates westward in a manner consistent with a downwelling Rossby wave that reaches BB3 in June (Fig. 12A). The onset of curl-driven downwelling in the southeastern Bay also occurs in May, so this wave-like reduction in primary production appears to be realized through the combined effects of the reflected spring Wyrtki Jet and local downward Ekman pumping.

Along 4.3 °N between 90 °E and 95 °E, the pattern of surface Chl$a$ exhibits reduced concentrations that also coincide directly with this downwelling wave (Fig. 12A). West of 90 °E, the spatial correspondence between production and surface Chl$a$ breaks down due to the opposing influence of the phytoplankton bloom associated with the SMC that advects into the Bay and dominates surface biological variability into the SWM/FIM transition (Figs. 2C, 3C, 8E and 12A). At BB3 in July, this advected bloom extends over the upper 75 m in the model (Fig. 12B). During the latter SWM, the surface bloom dissipates as the mixed layer deepens and euphotic zone nutrient availability decreases (Figs. 8F and 12B). This mixed-layer deepening and the accompanying biological response result from ongoing downward Ekman pumping at this location (data not shown). Values of modeled Chl$a$ at this time are lower than those in the SeaWiFS climatology (Fig. 8E). This could indicate that the SMC's influence is less persistent/extensive in the model and/or that the curl-induced downwelling and its biogeochemical effect are overemphasized.

3.2.5. Biogeochemical variability in the Southern Tropical Indian Ocean

While modeled Chl$a$ at ST1 is consistently higher than the SeaWiFS climatology (Fig. 13A), seasonal variability is consistent with the observations except during the FIM. The solution's SIM export flux maximum is not accompanied by a surface phytoplankton bloom but does coincide with nitrate that is notably higher than the NODC climatology (Figs. 13A, B). Otherwise, modeled nitrate coincides with the climatology. At ST2, SeaWiFS Chl$a$ remains below 0.2 mg/m^3 and exhibits little seasonal variability and modeled nitrate is consistent with the NODC climatology (Figs. 13C, D). During the NEM and SIM the low observed values of Chl$a$ are well represented in the model; however, a phytoplankton bloom that appears from the early SWM through the FIM is not accompanied by a notable increase in export flux (Fig. 13C). While model
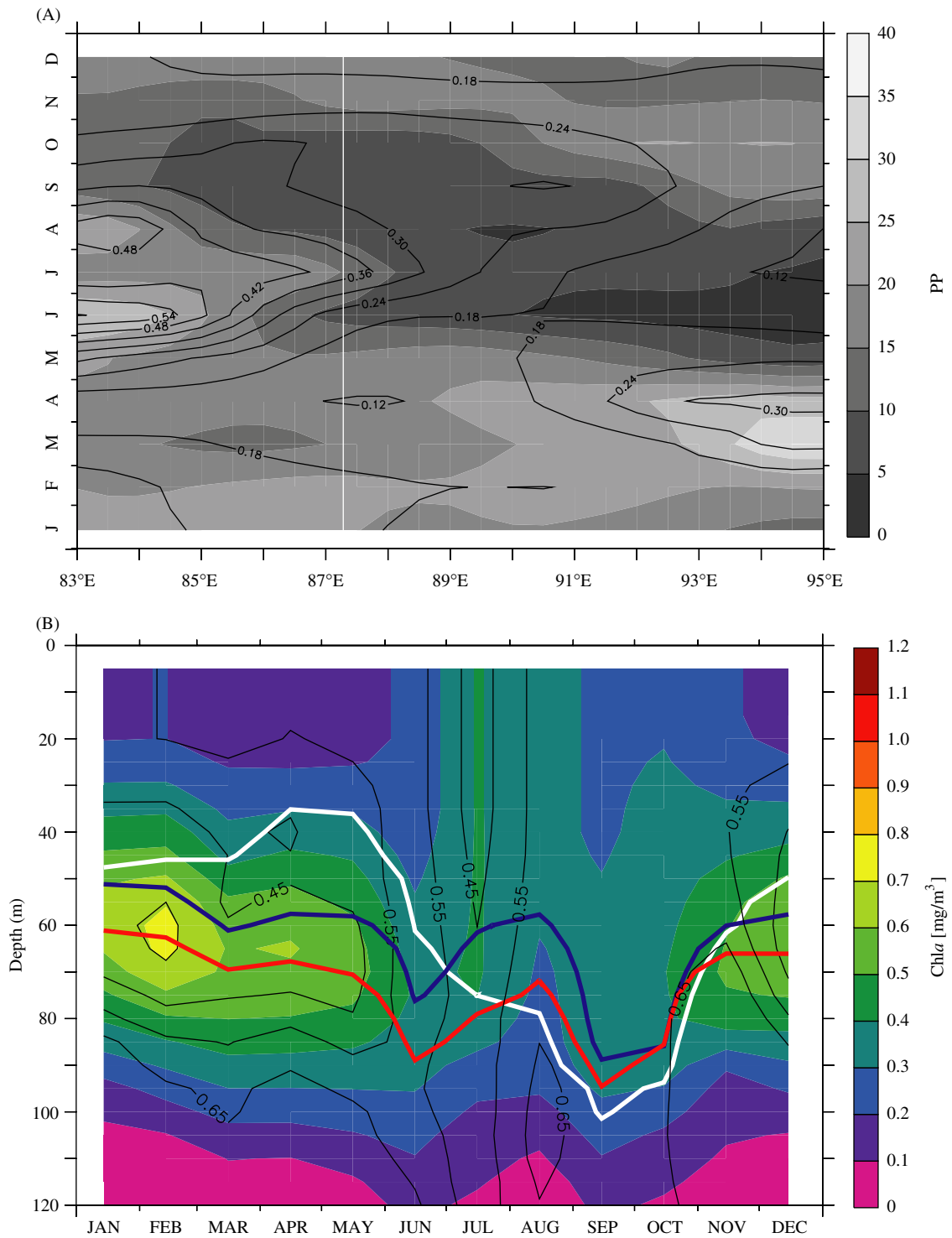
Fig. 12. (A) Vertically integrated primary production (mmol C/m² /d) along 4.3 °N in the southern Bay of Bengal. The superimposed contours are surface layer Chl$a$ (mg/m³). The white line represents the location of BB3. (B) Time series of Chl$a(z)$ over the upper 120 m at BB3. The superimposed contours are of $P_R(z)$. The blue line shows the temporal evolution of the 0.5 μM NO₃ isopleth. The red line shows the temporal evolution of the 50 pM iron isopleth. The white line shows the temporal evolution of mixed layer depth.
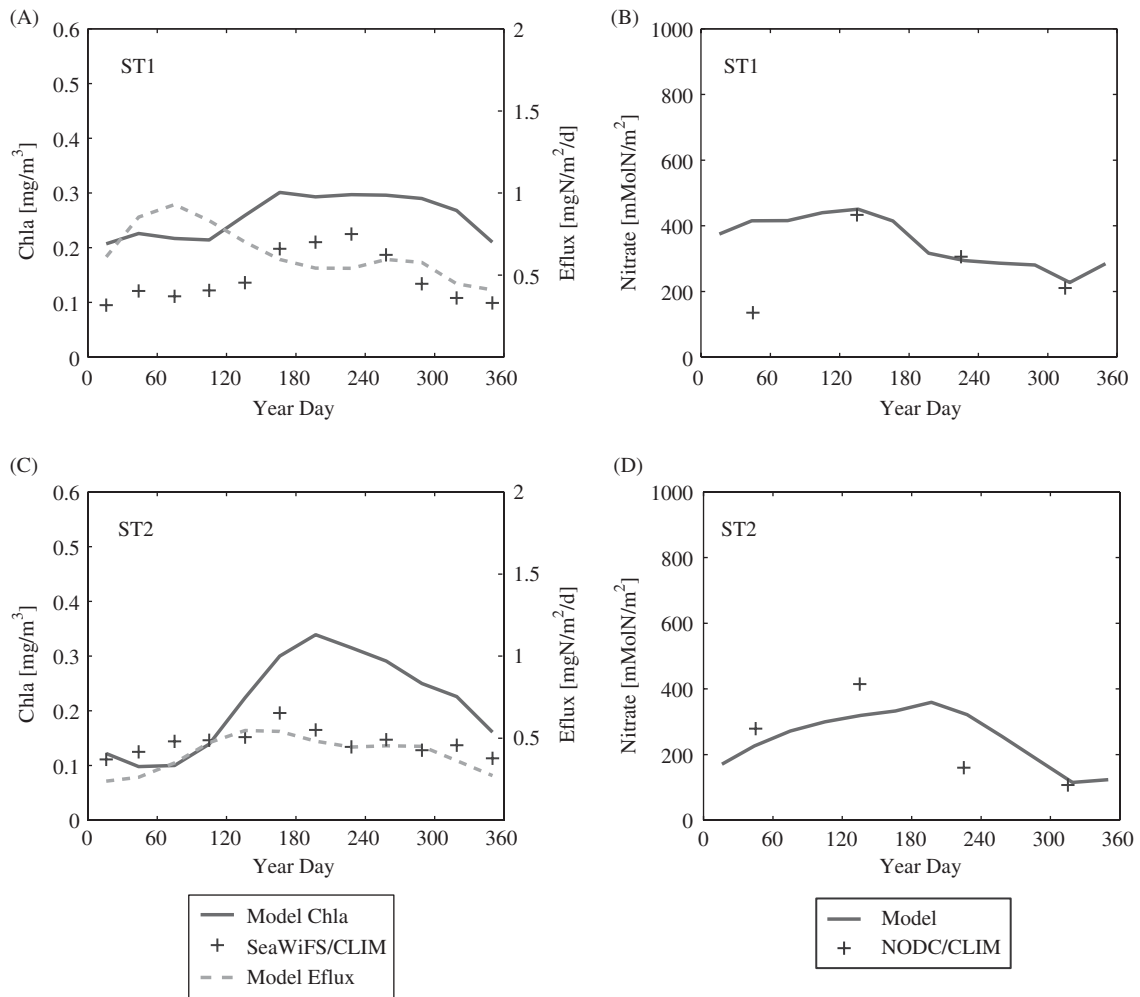
Fig. 13. Same as Fig. 10 but for the STIO (ST1 and ST2). The coordinates for the two sites are listed in Table 1.

export flux at the southern sites never exceeds $1\,\mathrm{mgN/m^2/d}$, both locations exhibit annual export that is comparable to, or higher than, annual export at the two equatorial sites (Table 3).

The 50 pM iron isopleth at ST1 and ST2 does not shoal above 50 m at either location, indicating that phytoplankton growth in the STIO is iron limited in the model (Figs. 14A, B). The lack of iron is reflected by the year-round dominance of the picoplankton (Figs. 14A, B) and the lowest peak rates of export flux around the basin (Table 3). The most pronounced phytoplankton feature at both locations is a generally persistent DCM, which only dissipates for a month or two during the SWM to FIM transition (Figs. 14A, B). At ST1, the DCM is shallower, intensifies earlier, and exhibits the region's only shift toward netplankton (Fig. 14A). This speciation shift

coincides with the annual peak in export flux (Fig. 13A). At ST2, the DCM tends to be deeper and more diffuse. It also exhibits lower Chl$a$, in part because surface Chl$a$ exceeds $0.3\,\mathrm{mg/m^3}$ for much of the SWM. As noted earlier, the SeaWiFS climatology indicates that the model's austral winter phytoplankton bloom is too prominent over the entire STIO (Figs. 2C, 3C and 13A, C).

Surface Chl$a$ across much of the STIO appears to coincide with westward-propagating Rossby waves or cross-basin distributions of local Ekman pumping. The temporal evolution of model nitracline depth anomaly indicates that Rossby waves influence upper-ocean nutrient availability throughout the year (Fig. 14C). During the NEM and SIM, the distribution of surface Chl$a$ closely tracks the Rossby wave-impacted variations in nitracline
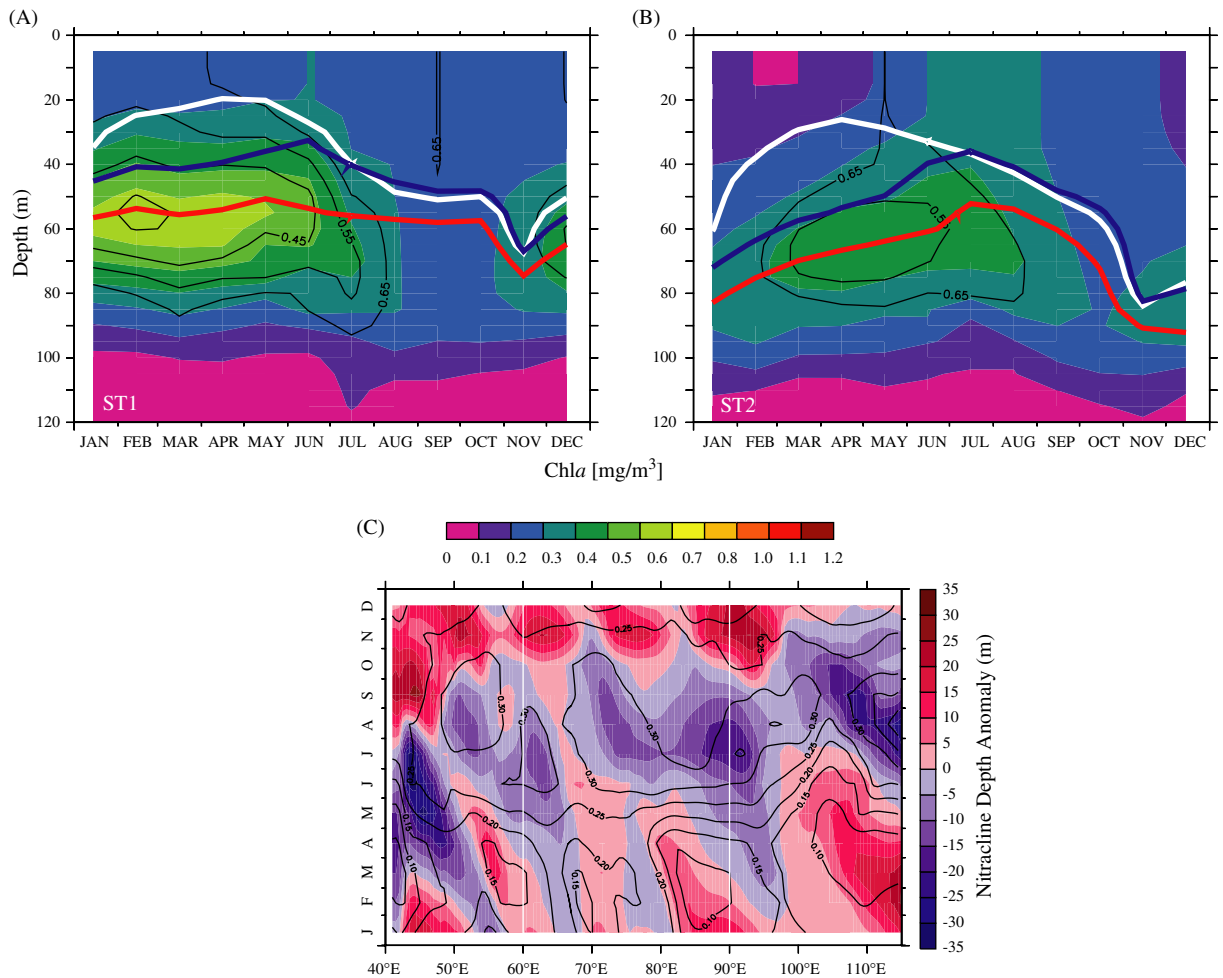
Fig. 14. Same as 12B but for (A) ST1 and (B) ST2. (C) Basinwide temporal evolution, along 10 °S, of nitracline depth anomaly with respect to the annual mean. The superimposed contours are surface layer Chla (mg/m³). The two white lines represent the latitudinal location of ST1 and ST2.

depth, with concentrations of ca. 0.2 mg/m³ aligning with the shoaling nitracline and lower concentrations aligning with the deepening nitracline. During the SWM and FIM, surface Chla is consistently > 0.25 mg/m³ over essentially the entire basin. The increased phytoplankton biomass is a response to persistently elevated Ekman pumping that prevails at this time and, while coincidence with wave-induced nitracline motions is still perceptible, the association between surface Chla and Rossby wave propagation in the model is less definitive.

3.3. Basinwide tendencies of most-limiting nutrient for netplankton growth

Significant spatial gradients in bioavailable iron are expected in the IO because of the distribution of

terrigenous dust sources around the basin (Prospero et al., 2002). The seasonal evolution of the surface ocean's most limiting nutrient for netplankton is shown in Fig. 15, with the red regions tending toward N-limitation (i.e. iron-replete) and the blue regions tending toward iron limitation. It should be emphasized here that these distributions illustrate limitation tendencies that will come into play should nutrients at a given location be fully utilized by netplankton. As noted earlier in Section 2.2 this reflects that fact that even though its concentration is elevated, iron in subsurface waters will be exhausted before nitrogen becomes limiting. Thus, these distributions indicate that netplankton growth in the surface ocean tends toward iron limitation when significant upwelling occurs if aeolian deposition does not provide significant additional enrichment.
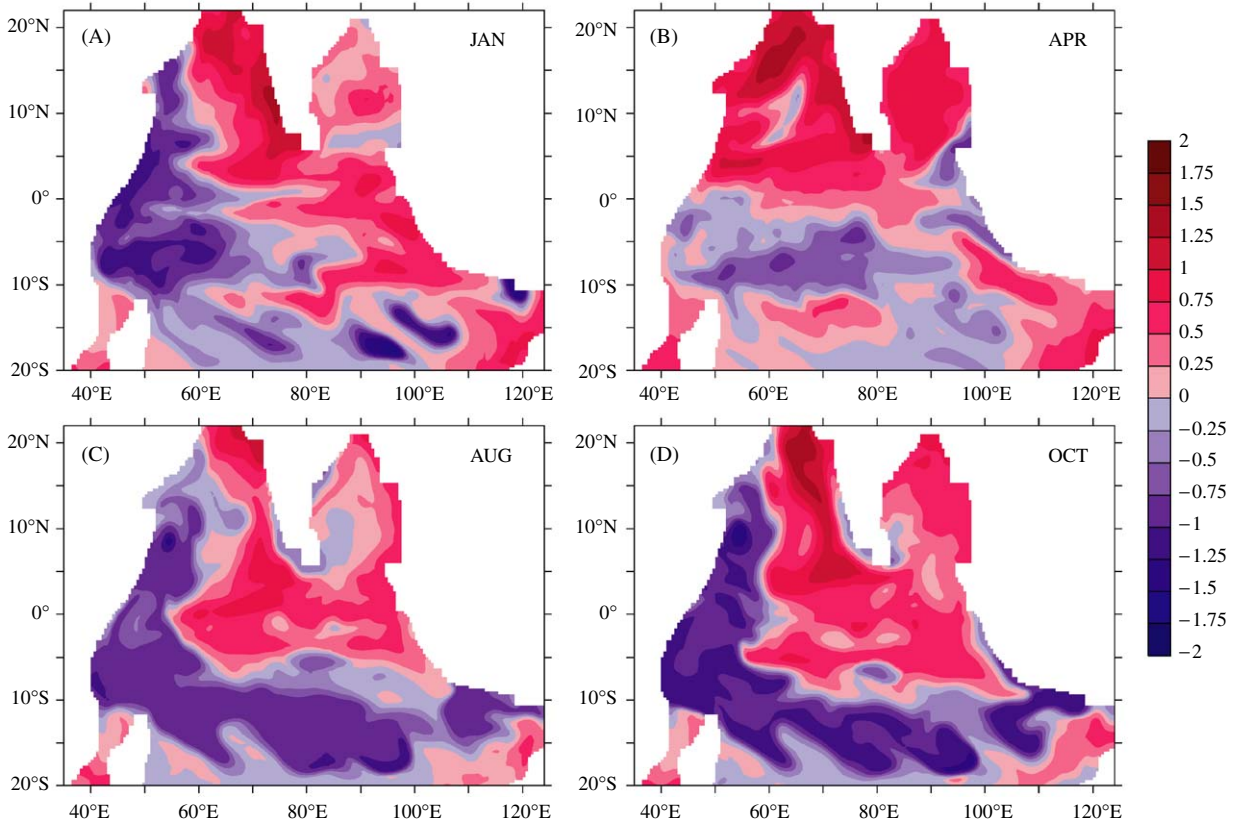
Fig. 15. Seasonal evolution of most limiting surface nutrient for netplankton (P_L), with blue (red) indicating Fe (N) limited netplankton growth (i.e., red is iron replete). The four seasons consist of (A) the NEM; (B) the SIM; (C) the SWM; and (D) the FIM. The plotted variable is the log transform of the ratio of the iron and nitrogen limitation functions $\log_{10}\left(L_{Fe}^L / \left(L_{NH_4}^L + L_{NO_3}^L\right)\right)$, where $L_{Fe}^L = \left[\frac{Fe}{K_{Fe}^L + Fe}\right]$, $L_{NH_4} = \left[\frac{NH_4}{K_{NH_4} + NH_4}\right]$ and $L_{NO_3}^L = \left[\left(1 - L_{NH_4}\right)\left(\frac{NO_3}{K_{NO_3}^L + NO_3}\right)\right]$.

The western Arabian Sea provides a prime example of the balance that exists between these two processes in the model. Coastal upwelling and Ekman pumping during the SWM and buoyancy driven convective mixing during the NEM drive surface waters toward iron limitation, and strong zonal gradients are apparent (Figs. 15A, C, and D). During the SIM, iron-replete conditions are restored except in the center of the region (Fig. 15B). The northern and eastern Arabian Sea is always iron replete, except along the southwest coast of India during the SWM and FIM. The Bay of Bengal remains iron replete, except in the southeast during the NEM and SIM (Figs. 15A, B). Surface waters associated with the Sri Lanka Dome east of Sri Lanka also tend toward iron limitation during the SWM and FIM. These areas in the southern Bay of Bengal tend toward iron limitation because of

upwelled waters that appear due to elevated Ekman pumping.

In the equatorial band west of 60 °E, iron limitation is indicated except during the SIM. During this period the model shows no strong tendency toward either iron or nitrogen limitation along the equator (Fig. 15B). However, a meridional gradient that signifies southward-increasing iron limitation tendency manifests west of 85 °E. From the equator to 10 °S the tendency toward iron limitation is widespread. In the STIO west of 60 °E, surface waters primarily tend toward iron limitation while iron-replete conditions are persistent in the east along the coasts of Sumatra and Australia. During the NEM iron limitation is indicated over the remainder of the STIO, except for a tongue that penetrates westward along 10 °S. Because of Ekman pumping during austral winter, the STIO south of

7 °S tends strongly toward iron limitation across the entire basin (Figs. 15C, D).

4. Discussion

Capturing the phytoplankton bloom dynamics of the Indian Ocean (IO), as well as accurately representing their relative inter-regional magnitudes and concomitant export fluxes, constitutes a significant modeling challenge. In the Arabian Sea, the model succeeds in capturing the oligotrophic nature of the SIM as well as the spatial extent of the regional phytoplankton blooms during the SWM and their subsequent retreat as the FIM progresses. Moreover, the timing and magnitude of the seasonal peaks in export flux that occur during the SWM are in good agreement with the observations (Figs. 7A, B), though, as also noted by Hood et al. (2003), high-frequency flux variability related to mesoscale activity is not realized. Over the entire basin, the model accurately simulates both the distribution of the SWM-period phytoplankton blooms and the contrast in magnitude between the blooms that develop in each region. The most notable shortcoming in Arabian Sea bloom dynamics occurs during the NEM at the three northernmost sites (AS1–AS3), where the winter bloom is too weak and the phytoplankton bloom that occurs in conjunction with the shoaling mixed layer during the transition from the NEM to the SIM is not well represented. The model also does not exhibit the secondary particle flux maxima apparent in the observations at AS2 and AS3.

The inconsistencies in Arabian Sea bloom dynamics during the NEM look to be primarily caused by an insufficient supply of surface nutrients, which is likely due to the lack of diurnal variability in the shortwave forcing. Inclusion of this high frequency forcing would allow the model to simulate better the diel mixed-layer oscillations that are known to occur. US JGOFS observations have revealed that elevated wintertime primary productivity occurs in conjunction with ongoing nitrate enrichment of surface waters (McCarthy et al., 1999; Barber et al., 2001). This atypical combination of processes has been shown to result from the co-occurrence of a relatively shallow permanent thermocline and the actively cycling mixed layer that promotes nutrient entrainment while preventing an accumulation of phytoplankton biomass in the euphotic zone (Wiggert et al., 2000). Subsequent efforts have demonstrated that incorporating such vertical os-

cillations improves the simulation of seasonal and interannual phytoplankton dynamics (McCreary et al., 2001; Wiggert et al., 2002).

During the most pronounced Arabian Sea monsoon blooms, Chla from both the model and the US JGOFS cruises is decidedly lower than the values in the SeaWiFS climatology. In the model this difference could relate to the transformation of phytoplankton biomass to Chla, while in the observations interannual and mesoscale variability could play a role. However, it is also well established that satellite chlorophyll retrievals are adversely impacted by high concentrations of absorbing aerosols (Moulin et al., 2001; Yoder et al., 2001), which are especially prominent during the SWM. Through the recent application of a spectral matching algorithm, significant improvements in SeaWiFS ocean color retrievals have been achieved over the Arabian Sea during high dust periods (Banzon et al., 2004). Their method provides a 75% increase in data return over the northern Arabian Sea and values of Chla that are up to 25% lower during the SWM, so the elevated SeaWiFS Chla values in Fig. 4 must be considered suspect (see also Kawamiya and Oschlies, 2003).

The comprehensive observational data acquired during the US JGOFS Arabian Sea Process Study provide for further assessment of the model's emulation of spatial heterogeneity and seasonal evolution in the ecosystem. In general, the model DCM tracks the appearance, intensification and dissipation of the DCM observed at the four JGOFS sites (Gundersen et al., 1998). The one notable exception occurs during the SIM at AS4 where the model DCM dissipates in association with a deep mixed layer while the observed DCM resides below a mixed layer of ~25 m. This difference can be attributed to the timing of mixed-layer shoaling, which occurs slightly later in the model. Otherwise, the seasonal evolution of the model DCM coincides with the observed behavior. However, Chla in the model DCM is consistently lower and usually ~15 m deeper, which suggests that the parameterization used to emulate low-light acclimation of phytoplankton N:Chl may not adequately represent this response. Low attenuation coefficients and/or too high photosynthetic rates at low light also could play a role.

The JGOFS observations reveal significant spatial heterogeneity in species distribution during the SWM that consists of increasing shoreward dominance of the larger phytoplankton (Savidge and

Gilpin, 1999; Tarran et al., 1999). In the model, the temporal evolution of $P_R(z)$ at AS2 and AS3 indicates the opposite spatial trend, as AS3 exhibits a pronounced shift toward netplankton during the August bloom while at AS2 picoplankton remain dominant throughout the SWM. At the latter location, PP is 2x higher and zooplankton biomass is 3x higher than observed during the JGOFS study (Table 2) and the 0.5 μM nitrate isopleth shoals starting in July whereas at AS3 it remains below 55 m (Fig. 6). The model does capture the observed shoreward increase in mesozooplankton dominance (Wishner et al., 1998; Stelfox et al., 1999) and features a shoreward gradient in total zooplankton biomass that is qualitatively correct, though stronger than observed (Table 2). These results indicate that a shift toward netplankton dominance is inhibited by iron limitation at AS2. Therefore, the model ecosystem with its elevated nutrient loads is more regenerative than in nature, which results in the too-high rates of productivity and zooplankton biomass. Overall, this suggests that coastally upwelled nutrients are not distributed as widely as they should be by lateral advection during the SWM. This is consistent with previous Arabian Sea modeling studies that emphasized the importance of accounting for the impact of mesoscale processes on offshore nutrient transport and ecosystem evolution during the SWM (Keen et al., 1997; Kawamiya, 2001), a conclusion that has been reinforced by recent JGOFS studies (Garrison et al., 1998; Lee et al., 2000; Fischer et al., 2002). As noted by Wiggert et al. (2005), at the present time the most significant advances in Arabian Sea biogeochemical modeling studies are likely to be realized by including finer spatial resolution that allows for the generation of the mesoscale phenomena (e.g., eddies and filaments) that appear prominently year-round.

The evolution of Great Whirl biogeochemical distributions in our solution as the SWM unfolds is largely consistent with that of McCreary et al. (1996). On the contrary, in the solution of Ryabchenko et al. (1998) the surface layer is deeper in May than in September. Thus the Great Whirl in their solution is less persistent and not as energetic, resulting in a less extensive redistribution of surface-layer phytoplankton. However, the Southern Gyre in the McCreary et al. (1996) solution has no distinct biological signature and, by August, has coalesced with the Great Whirl. In our solution, the Southern Gyre remains autonomous, with a distinct

set of biological signatures south of 3 °N. Based on the SeaWiFS climatology and the available observations of Somali Current biogeochemical characteristics, the spatio-temporal biological variability in our solution is more realistic. Differences in how the Somali Current system manifests and evolves could derive from various factors including model domain, grid resolution, vertical structure or applied wind forcing. The appearance and position of the Southern Gyre remains an open issue (Schott and McCreary, 2001). Numerical simulations have shown that its attributes are subject to significant, wind-induced interannual variability (Luther and O'Brien, 1989), which further suggests that the Southern Gyre's manifestation in OGCMs will be highly sensitive to variations or errors in applied wind forcing (see Esenkov et al., 2003).

The spatio-temporal evolution of the Somali Current and the Wyrtki Jets leads to dynamical features that exit their respective source regions and enter adjacent regions of the IO. This oceanic propagation results in dynamic inter-regional connections that can manifest as prominent biogeochemical responses to these remotely forced signals. The temporal evolution of biogeochemical processes in the southwestern Bay of Bengal is a primary example of such an inter-regional connection. In the model it is evident that during the SWM, this area is subject to the opposing influence of the downwelling Rossby wave that propagates in from the east and the phytoplankton bloom associated with the SMC that advects in from the west. The importance of inter-regional connections is further emphasized by a recent study that suggests that SMC-spawned mesoscale eddies in the Bay of Bengal contribute to euphotic zone nutrient enrichment via eddy pumping (Kumar et al., 2004), while earlier studies have demonstrated that westward-propagating Rossby waves exiting the Bay and entering the Arabian Sea can influence the Laccadive High (McCreary et al., 1993; Bruce et al., 1994). The latter connection could in turn contribute to establishing the anomalous thermocline conditions that have been associated with interannual variability in NEM-period Chla in the central Arabian Sea (Wiggert et al., 2002).

Along 10 °S in the STIO, the seasonal variability of surface Chla in the model results from a combination of remotely forced Rossby waves and the annual cycle in local Ekman pumping (Fig. 14). Eastward of 52 °E, curl-induced upwelling generally prevails north of 15 °S year-round, achieving its

annual maximum during austral winter. The seasonal variation in upwelling strength acts to modulate the degree to which variations in surface Chl*a* are related to passing Rossby waves. South of 15 °S, downward Ekman pumping prevails, with the annual downwelling maximum coinciding with the upwelling peak that occurs to the north. This spatial transition from persistent upwelling to persistent downwelling creates the pronounced hydrochemical front described by Longhurst (1998). In the model, as the magnitude of Ekman pumping decreases south of 10 °S, the correspondence between Rossby wave propagation and surface Chl*a* variability is amplified (data not shown). This contrasts the monotonic decrease from 5 °S to 30 °S in Chl*a* variance attributable to Rossby waves reported by Uz et al. (2001). This departure from observed behavior is a product of the too prominent SWM-period phytoplankton bloom noted earlier (Section 3.3.4) and suggests that the modeled STIO thermocline is too shallow. Taking into account the limiting nutrient distributions in Fig. 15, this further suggests that iron limitation in the STIO is more prevalent than the model presently indicates, and that primary productivity in this region relies on vertical transport of dissolved iron by Ekman pumping and planetary waves.

Explicitly simulating iron biogeochemistry is a recent development in ocean models (e.g., Christian et al., 2002b; Moore et al., 2002). At present, such efforts are hampered by the fact that concerted studies of oceanic iron are rather recent and evidence regarding several processes remains ambiguous (de Baar and de Jong, 2001, and references within). Validating model predicted iron concentrations is limited by: (1) sparse in situ observations; (2) the need to establish observational standards so analytical technique can be eliminated as a source of variability between data sets (Achterberg et al., 2001); and (3) the need for a straightforward means of interpreting iron concentration measurements in terms of bio-availability (Nishioka and Takeda, 2000). In the present model, euphotic zone sources of iron consist of aeolian deposition and upwelling/mixing from below. For application to the Indian Ocean, the maximum allowable subsurface iron concentration was increased to 750 pM, in accord with observations from the Arabian Sea (Takeda et al., 1995; Measures and Vink, 1999). To some degree, these measurements should reflect suboxic conditions that are generally located within 150 m of the surface over much of the northeastern Arabian

Sea (Morrison et al., 1999). Little is known regarding how quickly the elevated dissolved-iron carrying capacity of suboxic waters would decrease upon ventilation or mixing with oxygenated waters during upwelling and no provision for such a process has been included. Moreover, Arabian Sea iron conditions may not be typical of the basin as a whole; in their global study of oceanic iron demand Fung et al. (2000) used a higher N:Fe ratio in the southern IO than in the northern IO. Since the iron initial conditions in our simulations were uniformly applied over the model domain, regional iron availability could be overstated. Nevertheless, the surface-water iron-limitation tendencies suggested by the model should be representative of the actual spatio-temporal variability and inter-regional gradients, though the present characterizations of basinwide, in situ iron conditions are insufficient to corroborate or contest these results.

5. Conclusion

To our knowledge, this is the first bio-physical modeling study of the tropical Indian Ocean to report on biogeochemical processes over the entire basin. Simulation of the tropical Indian Ocean with a coupled bio-physical ocean model has provided several new insights into basin-scale biogeochemical processes. During the Southwest Monsoon, the basinwide spatial distribution of surface chlorophyll was accurately reproduced and biogeochemical variability in the Somali Current demonstrated notable improvement over previous modeling efforts. The model suggests that iron limitation is widespread in the western and southern portions of the Indian Ocean, and may even occur in the Arabian Sea under strong upwelling conditions. The eastward progression of the semiannual Wyrtki Jets was shown to be a primary contributor to equatorial biogeochemical variability through its deepening of the eastern nitracline. The model demonstrated that the propagation of the Somali Current and the spring Wyrtki Jet beyond their respective source regions results in significant, yet opposing, effects on ecosystem variability in the southern Bay of Bengal during the SWM. The model also demonstrated that in the STIO, local Ekman pumping and remotely forced Rossby waves combine as the means for supplying nutrients, in particular dissolved iron, to the euphotic zone. The impact of these dynamical features on biogeochemical variability via inter-regional connections underscores the

need to further characterize these linkages and suggests that ongoing advancement of our understanding of biogeochemical processes in the tropical Indian Ocean requires a basinwide perspective.

Acknowledgements

Appendix A

The August SeaWiFS climatology reveals a marked contrast between surface Chl*a* in the northern Arabian Sea and the STIO (Fig. 2C). Initial numerical experiments that utilized the original Equatorial Pacific configuration of the model did not exhibit this basinwide contrast, with the most pronounced bloom being associated with the Southern Gyre. Moreover, a 1-D version of the ecosystem model was among a group of models included in the so-called Arabian Sea Testbed (AST) within which a consistent physical framework from the central Arabian Sea has been applied (Friedrichs et al., 2006). One conclusion that emerged from our initial work with the AST was that the applied zooplankton grazing coefficients prevented the observed dynamic range in Arabian Sea phytoplankton blooms from developing. To promote phytoplankton bloom formation, these grazing coefficients were lowered and hyperbolic mortality of netplankton (P_L) and macrozooplankton (Z_L) was incorporated. In addition, zooplankton grazing on detritus was introduced. The inclusion of hyperbolic closure has been demonstrated to improve NPZ model behavior (Steele and Henderson, 1992; Edwards and Yool, 2000), while support for the inclusion of coprophagy comes from both zooplankton grazing studies (e.g., Roman, 1984; Huskin et al., 2004) and ecosystem model stability analyses (Edwards, 2001).

The inclusion of these processes required modified versions of five of the ecosystem equations originally documented by Christian et al. (2002a). The modified forms of these equations appear below (Eqs. (A.1)–(A.3)). Changes in the parameter set, and the values of several additional parameters necessitated by the modified equations appear in Table 4. Following Friedrichs (2002), a measure of model misfit $\Psi = 100^* \langle |X_{\mathrm{MOD}} - X_{\mathrm{OBS}}|/X_{\mathrm{OBS}} \rangle$ was defined as the mean percent difference between the model and available observations for all data pairs of a given variable. Model misfit is calculated for five variables (PP, PON, zooplankton biomass, export production and surface Chl*a*). The temporal scale is seasonal for the three process study variables (Table 2), while for export production (Table 3) and SeaWiFS Chl*a* (Fig. 4) it is annual and monthly, respectively. For this sensitivity analysis, output from year 4 of the standard run and the five comparison cases are used. The standard run employs the parameter set in Table 4 and the equations listed below, along with the remaining unchanged parameters and equations (Christian et al., 2002a).

Netplankton (P_L):

$$\frac{\partial P_L}{\partial t} = \mu_{\max}(T)f(E)g(\mathrm{NO}_3^-, \mathrm{NH}_4^+, \mathrm{Fe})P_L$$
$$- g_{P_L}\Lambda(1 - \mathrm{e}^{-\Lambda P_L})P_L Z - mP_L\left(\frac{P_L}{K_{P_L} + P_L}\right).$$
(A.1)

Microzooplankton (Z_S):

$$\frac{\partial Z_S}{\partial t} = Z_S\Big(\lambda\Lambda\big(g_{P_S}(1 - \mathrm{e}^{-\Lambda P_S})P_S + g_{D_S}(1 - \mathrm{e}^{-\Lambda D_S})D_S\big)$$
$$- g_{Z_S}\Lambda(1 - \mathrm{e}^{-\Lambda Z_S})Z_L - r_S - \delta_S\Big).$$
(A.2a)

Macrozooplankton (Z_L):

$$\frac{\partial Z_L}{\partial t} = Z_L\lambda\Lambda\Big(g_{P_L}(1 - \mathrm{e}^{-\Lambda P_L})P_L$$
$$+ g_{Z_S}(1 - \mathrm{e}^{-\Lambda Z_S})Z_S + g_{D_L}(1 - \mathrm{e}^{-\Lambda D_L})D_L\Big)$$
$$- Z_L\left(r_L + \delta_L\left(\frac{Z_L}{K_{Z_L} + Z_L}\right)\right).$$
(A.2b)

Detritus equations:

$$\frac{\partial D_S}{\partial t} = (1 - \lambda)\Lambda\Big(g_{P_S}(1 - \mathrm{e}^{-\Lambda P_S})P_S Z_S$$
$$+ g_{D_L}(1 - \mathrm{e}^{-\Lambda D_L})D_L Z_L\Big) + \delta_S Z_S + m_S P_S$$
$$- \Big(\lambda g_{D_S}\Lambda(1 - \mathrm{e}^{-\Lambda D_S})Z_S + c_S + w_S\Big)D_S.$$
(A.3a)

Table 4
Values of ecosystem model parameters that have been altered from those applied in Christian et al. (2002a)

Symbol	Description	Unit	Small	Large
K_{NO_3}	Half-saturation for nitrate uptake	μM	0.4	0.8
K_{NH_4}	Half-saturation for ammonium uptake	μM	0.05	0.05
K_{Fe}	Half-saturation for iron uptake	PM	25	120
R	Molar iron-to-nitrogen ratio	Dimensionless	3.30E−05	6.70E−05
gP_S, gP_L	Phytoplankton grazing coefficient	d^{-1}	10	2
gZ_S	Microzooplankton grazing coefficient	d^{-1}	2	NA
gD_S, gD_L	Detritus grazing coefficient	d^{-1}	2	0.4
δ_S, δ_L	Zooplankton nongrazing mortality rate	d^{-1}	0.05	0.4
K_{P_L}	Half-saturation for quadratic netplankton mortality	μM	NA	0.1
K_{Z_L}	Half-saturation for quadratic macrozooplankton mortality	μM	NA	0.1
c_S, c_L	Detrital remineralization rate	D^{-1}	0.0335	0.0335
w_S, w_L	Specific loss rate of detritus to sedimentation	d^{-1}	0.025	0.098
k_w	Light attenuation by seawater	m^{-1}	0.0313	0.0313

The parameter K_{NH_4} is unchanged but has been included for completeness since it appears in the definition of L_{NH_4} (see caption for Fig. 15). The bold italic symbols indicate additional parameters introduced with the modifications that were incorporated into the ecosystem equations (Eqs. (A.1)–(A.3)).

$$\frac{\partial D_L}{\partial t} = (1-\lambda)\Lambda\Big(g_{P_L}\big(1-e^{-\Lambda P_L}\big)P_L + g_{Z_S}$$
$$\times \big(1-e^{-\Lambda Z_S}\big)Z_S\Big)Z_L + \delta_L Z_L\left(\frac{Z_L}{K_{Z_L}+Z_L}\right)$$
$$+ mP_L\left(\frac{P_L}{K_{P_L}+P_L}\right)$$
$$- \Big(g_{D_L}\Lambda\big(1-e^{-\Lambda D_L}\big)Z_L + c_L + w_L\Big)D_L.$$
$$(A.3b)$$

The five alternative model solutions are as follows. Case 1 is the original Equatorial Pacific configuration (Christian et al., 2002a). For Case 2, all grazing coefficients (i.e., $g_{P_S}, g_{P_L}, g_{Z_S}, g_{D_S}, g_{D_L}$) are increased by 20%. For Cases 3 and 4, linear mortality of netplankton and macrozooplankton respectively is reestablished by setting K_{P_L} or K_{Z_L} to zero. For Case 5, grazing on detritus is removed by setting g_{D_S} and g_{D_L} to zero. The normalized model misfit $\Psi^* = \Psi/\Psi_{ST}$, where Ψ_{ST} represents the standard model run, for each of the five variables is listed in Table 5. There is always at least one variable for which the standard case provides a significantly better representation. Case 1 (original Equatorial Pacific configuration) has the poorest correspondence to SeaWiFS Chla and export production, but the best correspondence to zooplankton biomass. Uniformly increasing grazing in the model by 20% (Case 2) resulted in only small departures from the standard case (i.e., $\Psi^* = 1$; only for export flux does Ψ deviate by more than 10% from the standard run.

Table 5
Values of model misfit for the standard run (Ψ_{ST}) and the normalized values of model misfit (Ψ^*) that illustrate the impact of the various model parameter adjustments and equation modifications

	Ψ_{ST} (Standard)	Ψ^*				
		Case 1	Case 2	Case 3	Case 4	Case 5
JGOFS PP	43.1	0.89	0.95	1.26	0.90	1.13
JGOFS PON	25.1	1.05	0.98	0.95	0.99	1.20
JGOFS TotalZ	90.1	0.46	0.98	1.77	1.03	0.56
JGOFS Export	23.2	2.03	1.30	0.86	1.57	0.42
SeaWiFS Chla	35.8	1.69	1.09	1.10	1.03	0.90

Values of Ψ^* greater than one demonstrate that a given case performs worse than the standard run. Definitions for Ψ^* and Ψ_{ST} are provided in the appendix. The five observational data sets (JGOFS PP, JGOFS PON, JGOFS Zooplankton biomass, JGOFS Export and SeaWiFS Chla) are described in the text.

The last three cases illustrate the impact of the changes made to the ecosystem model's structure. Case 3 consists of restoring the netplankton mortality term to its original linear form (Eqs. (A.1) and (A.3b)) and results in the worst correspondence to PP and zooplankton biomass. While larger phytoplankton blooms did manifest with the hyperbolic form, Ψ^* for Chla was near 1. This suggests that Chla during non-bloom periods was better represented when applying the linear netplankton mortality formulation, offsetting the impact on Ψ^* during bloom periods. The linear form results in an ecosystem that is more

regenerative, as indicated by a reduction in f-ratio of approximately 20% (not shown).

Case 4 consists of restoring the macrozooplankton mortality term to linear form (Eqs. (A.2b) and (A.3b)). As expected, this strongly impacts the vertical flux of organic matter. For export Case 4 exhibits poorer correspondence with the observations, with the linear mortality configuration resulting in export rates that are consistently too low. For the other fields, the Case 4 solution is always within 10% of the standard solution.

Case 5 consists of removing the grazing of detritus by zooplankton by setting g_{D_S} and g_{D_L} to zero (Eqs. (A.2) and (A.3)). Both PP and PON are negatively impacted by this configuration, with the two variables showing just over 10% and 20% poorer correspondence, respectively. On the other hand, Case 5 exhibits significantly better correspondence with the observations of zooplankton biomass and export. Overall, sensitivity to the inclusion or exclusion of this process is low.

This exploration of alternative forms was motivated by a need to improve the model's representation of the basinwide variation in surface Chl*a* associated with SWM-period phytoplankton blooms. This was achieved, and simulation of export flux as observed by sediment traps also improved. Each modification was also tested individually in order to ascertain their specific impact. All were found to produce significant improvements in the model-data misfit, except for allowing zooplankton to graze on detritus (Case 5), which improved the realization of PON, but worsened total zooplankton biomass and export flux.

References

Achterberg, E.P., Holland, T.W., Bowie, A.R., Fauzi, R., Mantoura, C., Worsfold, P.J., 2001. Determination of iron in seawater. Analytica Chimica Acta 442, 1–14.

Antonov, J., Levitus, S., Boyer, T. P., Conkright, M., O'Brien, T., Stephens, C., Trotsenko, B., 1998. World Ocean Atlas 1998, vol. 3, Temperature of the Indian Ocean. NOAA Atlas NESDIS 29. U.S. Gov. Printing Office, Washington DC, (166pp).

Banse, K., 1994. On the coupling of hydrography, phytoplankton, zooplankton, and settling organic particles offshore in the Arabian Sea. Proceedings of the Indian Academy Science—Earth and Planetary Science 103, 125–161.

Banse, K., McClain, C.R., 1986. Winter blooms of phytoplankton in the Arabian Sea as observed by the Coastal Zone Color Scanner. Marine Ecological Progress Series 34, 201–211.

Banzon, V.F., Evans, R.E., Gordon, H.R., Chomko, R.M., 2004. SeaWIFS observations of the Arabian Sea Southwest Monsoon bloom for the year 2000. Deep-Sea Research II 51, 189–208.

Barber, R.T., Marra, J., Bidigare, R.C., Codispoti, L.A., Halpern, D., Johnson, Z., Latasa, M., Goericke, R., Smith, S.L., 2001. Primary productivity and its regulation in the Arabian Sea during 1995. Deep-Sea Research II 48, 1127–1172.

Bhat, G.S., et al., 2001. BOBMEX: the Bay of Bengal monsoon experiment. Bulletein of the American Meterogical Society 82, 2217–2243.

Boyer, T.P., Levitus, S., Antonov, J., Conkright, M., T., O.B., Stephens, C., Trotsenko, B., 1998. World Ocean Atlas 1998, vol. 6, Salinity of the Indian Ocean. NOAA Atlas NESDIS 32. US Gov. Printing Office, Washington, DC, 166pp.

Brock, J.C., McClain, C.R., 1992. Interannual variability in phytoplankton blooms observed in the Northwestern Arabian Sea during the Southwest Monsoon. Journal of Geophysical Research 97, 733–750.

Bruce, J.G., Johnson, D.R., Kindle, J.C., 1994. Evidence for eddy formation in the eastern Arabian Sea during the northeast monsoon. Journal of Geophysical Research 99, 7651–7664.

Chen, D., Busalacchi, A., Rothstein, L., 1994. The roles of vertical mixing, solar radiation, and wind stress in a model simulation of the sea surface temperature seasonal cycle in the tropical Pacific Ocean. Journal of Geophysical Research 99, 20,345–20,359.

Christian, J.R., Murtugudde, R., 2003. Tropical Atlantic variability in a coupled physical-biogeochemical ocean model. Deep-Sea Research II 50, 2947–2969.

Christian, J.R., Verschell, M.A., Murtugudde, R., Busalacchi, A.J., McClain, C.R., 2002a. Biogeochemical modelling of the tropical Pacific Ocean I: seasonal and interannual variability. Deep-Sea Research II 49, 509–543.

Christian, J.R., Verschell, M.A., Murtugudde, R., Busalacchi, A.J., McClain, C.R., 2002b. Biogeochemical modelling of the tropical Pacific Ocean II: iron biogeochemistry. Deep-Sea Research II 49, 545–565.

Cipollini, P., Cromwell, D., Challenor, P.G., Raffaglio, S., 2001. Rossby waves detected in global ocean colour data. Geophysical Research Letter 28, 323–326.

Conkright, M., O'Brien, T., Levitus, S., Boyer, T.P., Antonov, J., Stephens, C., 1998. World Ocean Atlas 1998, vol. 12, Nutrients and Chlorophyll of the Indian Ocean. NOAA Atlas NESDIS 38. U.S. Gov. Printing Office, Washington, DC, 217pp.

de Baar, H.J.W., de Jong, J.T.M., 2001. Distributions, sources and sinks of iron in seawater. In: D.R. Turner, K.A. Hunter, (Eds.), The Biogeochemistry of Iron in Seawater. Wiley, Newyork, pp. 123–253.

Edwards, A.M., 2001. Adding detritus to a nutrient-phytoplankton-zooplankton model: a dynamical-systems approach. Journal of Plankton Research 23, 389–413.

Edwards, A.M., Yool, A., 2000. The role of higher predation in plankton population models. Journal of Plankton Research 22, 1085–1112.

Esenkov, O.E., Olson, D.B., Bleck, R., 2003. A study of the circulation and salinity budget of the Arabian Sea with an isopycnic coordinate ocean model. Deep-Sea Research II 50, 2091–2110.

Fischer, A.S., Weller, R.A., Rudnick, D.L., Eriksen, C.C., Lee, C.M., Brink, K.H., Fox, C.A., Leben, R.R., 2002. Mesoscale eddies, coastal upwelling, and the upper-ocean heat budget in the Arabian Sea. Deep-Sea Research II 49, 2231–2264.

Fischer, J., Schott, F., Stramma, L., 1996. Currents and transports of the Great Whirl Socotra Gyre system during the summer monsoon, August 1993. Journal of Geophysical Research 101, 3573–3587.

Friedrichs, M.A.M., 2002. Assimilation of JGOFS EqPac and SeaWiFS data into a marine ecosystem model of the central equatorial Pacific Ocean. Deep-Sea Research II 49, 289–319.

Friedrichs, M.A.M., Hood, R.R., Wiggert, J.D., 2006. Ecosystem model complexity versus physical forcing: quantification of their relative impact with assimilated Arabian Sea data. Deep-Sea Research II this volume [doi:10.1016/j.dsr2.2006.01.026].

Fung, I.Y., Meyn, S.K., Tegen, I., Doney, S.C., John, J.G., Bishop, J.K.B., 2000. Iron supply and demand in the upper ocean. Global Biogeochemical Cycles 14, 281–295.

Garrison, D.L., Gowing, M.M., Hughes, M.P., 1998. Nano- and microplankton in the northern Arabian Sea during the Southwest Monsoon, August–September 1995—a US-JGOFS study. Deep-Sea Research II 45, 2269–2299.

Ginoux, P., Chin, M., Tegen, I., Prospero, J.M., Holben, B., Dubovik, O., Lin, S.J., 2001. Sources and distributions of dust aerosols simulated with the GOCART model. Journal of Geophysical Research 106, 20255–20273.

Gundersen, J.S., Gardner, W.D., Richardson, M.J., Walsh, I.D., 1998. Effects of monsoons on the seasonal and spatial distributions of POC and chlorophyll in the Arabian Sea. Deep-Sea Research II 45, 2103–2132.

Hitchcock, G.L., Key, E.L., Masters, J., 2000. The fate of upwelled waters in the Great Whirl, August 1995. Deep-Sea Research II 47, 1605–1621.

Honjo, S., Dymond, J., Prell, W., Ittekkot, V., 1999. Monsoon-controlled export fluxes to the interior of the Arabian Sea. Deep-Sea Research II 46, 1859–1902.

Hood, R.R., Kohler, K.E., McCreary, J.P., Smith, S.L., 2003. A four-dimensional validation of a coupled physical–biological model of the Arabian Sea. Deep-Sea Research II 50, 2917–2945.

Huskin, I., Viesca, L., Anadón, R., 2004. Particle flux in the Subtropical Atlantic near the Azores: influence of mesozooplankton. Journal of Plankton Research 26, 403–415.

Ittekkot, V., Nair, R.R., Honjo, S., Ramaswamy, V., Bartsch, M., Manganini, S., Desai, B.N., 1991. Enhanced particle fluxes in Bay of Bengal induced by injection of fresh water. Nature 351, 385–387.

Jickells, T.D., Spokes, L.J., 2001. Atmospheric Iron Inputs to the Oceans. In: Turner, D.R., Hunter, K.A. (Eds.), The Biogeochemistry of Iron in Seawater. Wiley, Newyork, pp. 123–253.

Kalnay, E., et al., 1996. The NCEP/NCAR 40-year reanalysis project. Bulletin of the American Meterological Society 77, 437–471.

Kawamiya, M., 2001. Mechanism of offshore nutrient supply in the western Arabian Sea. Journal of Marine Research 59, 675–696.

Kawamiya, M., Oschlies, A., 2001. Formation of a basin-scale surface chlorophyll pattern by Rossby waves. Geophysical Research Letters 28, 4139–4142.

Kawamiya, M., Oschlies, A., 2003. An eddy-permitting, coupled ecosystem-circulation model of the Arabian Sea: comparison with observations. Journal of Marine System 38, 221–257.

Keen, T.R., Kindle, J.C., Young, D.K., 1997. The interaction of southwest monsoon upwelling, advection and primary production in the northwest Arabian Sea. Journal of Marine System 13, 61–82.

Kumar, S.P., Muraleedharan, P.M., Prasad, T.G., Gauns, M., Ramaiah, N., de Souza, S.N., Sardesai, S., Madhupratap, M., 2002. Why is the Bay of Bengal less productive during summer monsoon compared to the Arabian Sea? Geophysical Research Letters 29, doi:10.1029/2002GL016013.

Kumar, S.P., Murukesh, N., Narvekar, J., Kumar, A., Sardesai, S., de Souza, S. N., Gauns, M., Ramaiah, N., Madhupratap, M., 2004. Are eddies nature's trigger to enhance biological productivity in the Bay of Bengal? Geophysics Research Letters 31, doi:10.1029/2003GL019274.

Landry, M.R., Brown, S.L., Campbell, L., Constantinou, J., Liu, H.B., 1998. Spatial patterns in phytoplankton growth and microzooplankton grazing in the Arabian Sea during monsoon forcing. Deep-Sea Research II 45, 2353–2368.

Latasa, M., Bidigare, R.R., 1998. A comparison of phytoplankton populations of the Arabian Sea during the Spring Intermonsoon and Southwest Monsoon of 1995 as described by HPLC-analyzed pigments. Deep-Sea Research II 45, 2133–2170.

Lee, C.M., Jones, B.H., Brink, K.H., Fischer, A.S., 2000. The upper-ocean response to monsoonal forcing in the Arabian Sea: seasonal and spatial variability. Deep-Sea Research II 47, 1177–1226.

Leonard, C.L., McClain, C.R., Murtugudde, R., Hofmann, E.E., Harding Jr., L.W., 1999. An iron-based ecosystem model of the central equatorial Pacific. Journal of Geophysical Research 104, 1325–1341.

Longhurst, A., 1998. Ecological Geography of the Sea. Academic Press, San Diego (398pp).

Luther, M.E., O'Brien, J.J., 1989. Modelling the variability in the Somali Current. In: Nihoul, J.C.J., Jamart, B.M. (Eds.), Mesoscale/Synoptic Coherent Structures in Geophysical Turbulence. Elsevier, Amesterdam, pp. 373–386.

Madhupratap, M., Gauns, M., Ramaiah, N., Prasanna Kumar, S., Muraleedharan, P.M., de Sousa, S.N., Sardessai, S., Muraleedharan, U., 2003. Biogeochemistry of the Bay of Bengal: physical, chemical and primary productivity characteristics of the central and western Bay of Bengal during summer monsoon 2001. Deep-Sea Research II 50, 881–896.

Madhupratap, M., Kumar, S.P., Bhattathiri, P.M.A., Kumar, M.D., Raghukumar, S., Nair, K.K.C., Ramaiah, N., 1996. Mechanism of the biological response to winter cooling in the northeastern Arabian Sea. Nature 384, 549–552.

Martin, J.H., Knauer, G.A., Karl, D.M., Broenkow, W.W., 1987. VERTEX: carbon cycling in the northeast Pacific. Deep-Sea Research I 34, 267–285.

McCarthy, J.J., Garside, C., Nevins, J.L., 1999. Nitrogen dynamics during the Arabian Sea Northeast Monsoon. Deep-Sea Research II 46, 1623–1664.

McCreary, J.P., Kohler, K.E., Hood, R.R., Olson, D.B., 1996. A four-component model of biological activity in the Arabian Sea. Progress in Oceanography 37, 193–240.

McCreary, J.P., Kohler, K.E., Hood, R.R., Smith, S., Kindle, J., Fischer, A.S., Weller, R.A., 2001. Influences of diurnal and intraseasonal forcing on mixed-layer and biological variability

in the central Arabian Sea. Journal of Geophysical Research 106, 7139–7155.

McCreary, J.P., Kundu, P.K., Molinari, R.L., 1993. A numerical investigation of dynamics, thermodynamics and mixed-layer processes in the Indian Ocean. Progress in Oceanography 31, 181–244.

Measures, C.I., Vink, S., 1999. Seasonal variations in the distribution of Fe and Al in the surface waters of the Arabian Sea. Deep-Sea Research II 46, 1597–1622.

Moore, J.K., Doney, S.C., Glover, D.M., Fung, I.Y., 2002. Iron cycling and nutrient-limitation patterns in surface waters of the World Ocean. Deep-Sea Research II 49, 463–507.

Morrison, J.M., et al., 1999. The oxygen minimum zone in the Arabian Sea during 1995. Deep-Sea Research II 46, 1903–1931.

Moulin, C., Gordon, H.R., Chomko, R.M., Banzon, V.F., Evans, R.H., 2001. Atmospheric correction of ocean color imagery through thick layers of Saharan dust. Geophysical Research Letters 28, 5–8.

Murtugudde, R., Busalacchi, A.J., 1999. Interannual variability of the dynamics and thermodynamics of the tropical Indian Ocean. Journal of Climate 12, 2300–2326.

Murtugudde, R., McCreary, J.P., Busalacchi, A.J., 2000. Oceanic processes associated with anomalous events in the Indian Ocean with relevance to 1997–1998. Journal of Geophysical Research 105, 3295–3306.

Murtugudde, R.G., Signorini, S.R., Christian, J.R., Busalacchi, A.J., McClain, C.R., Picaut, J., 1999. Ocean color variability of the tropical Indo-Pacific basin observed by SeaWiFS during 1997–1998. Journal of Geophysical Research 104, 18351–18366.

Nishioka, J., Takeda, S., 2000. Change in the concentrations of iron in different size fractions during growth of the oceanic diatom Chaetoceros sp: importance of small colloidal iron. Marine of Biology 137, 231–238.

Oberhuber, J., 1998. An atlas based on COADS data set. Report 15. Max Plank Institut für Meteorol. Hamburg, Germany (182pp).

Prospero, J.M., Ginoux, P., Torres, O., Nicholson, S.E., Gill, T.E., 2002. Environmental characterization of global sources of atmospheric soil dust identified with the NIMBUS7 (TOMS) absorbing aerosol product. Reviews of Geophysics 40, 1–31.

Ramaswamy, V., Nair, R.R., 1994. Fluxes of material in the Arabian Sea and Bay of Bengal—sediment trap studies. Proceedings of the Indian Academy of Science-Earth and Planetary Science 103, 189–210.

Roman, M., Smith, S., Wishner, K., Zhang, X.S., Gowing, M., 2000. Mesozooplankton production and grazing in the Arabian Sea. Deep-Sea Research II 47, 1423–1450.

Roman, M.R., 1984. Utilization of detritus by the copepod, *Acartia tonsa*. Limnology and Oceanography 29, 949–959.

Ryabchenko, V.A., Gorchakov, V.A., Fasham, M.J.R., 1998. Seasonal dynamics and biological productivity in the Arabian Sea euphotic zone as simulated by a three-dimensional ecosystem model. Global Biogeochemical Cycles 12, 501–530.

Saager, P.M., Debaar, H.J.W., Burkill, P.H., 1989. Manganese and iron in Indian Ocean waters. Geochimica Et Cosmochimica Acta 53, 2259–2267.

Saji, N.H., Goswami, B.N., Vinayachandran, P.N., Yamagata, T., 1999. A dipole mode in the tropical Indian Ocean. Nature 401, 360–363.

Savidge, G., Gilpin, L., 1999. Seasonal influences on size-fractionated chlorophyll *a* concentrations and primary production in the north-west Indian Ocean. Deep-Sea Research II 46, 701–723.

Schott, F., 1983. Monsoon response of the Somali Current and associated upwelling. Progress in Oceanography 12, 357–381.

Schott, F.A., McCreary, J.P., 2001. The monsoon circulation of the Indian Ocean. Progress in Oceanography 51, 1–123.

Seager, R., Blumenthal, M., Kushnir, Y., 1995. An advective atmospheric mixed layer model for ocean modeling purposes: global simulation of surface heat fluxes. Journal of Climate 8, 1951–1964.

Smith, S., Roman, M., Prusova, I., Wishner, K., Gowing, M., Codispoti, L.A., Barber, R., Marra, J., Flagg, C., 1998a. Seasonal response of zooplankton to monsoonal reversals in the Arabian Sea. Deep-Sea Research II 45, 2369–2403.

Smith, S.L., Codispoti, L.A., 1980. Southwest Monsoon of 1979: chemical and biological response of somali coastal waters. Science 209, 597–600.

Smith, S.L., Codispoti, L.A., Morrison, J.M., Barber, R.T., 1998b. The 1994-1996 Arabian Sea Expedition: an integrated, interdisciplinary investigation of the response of the northwestern Indian Ocean to monsoonal forcing. Deep-Sea Research II 45, 1905–1915.

Steele, J.H., Henderson, E.W., 1992. The role of predation in plankton models. Journal of Plankton Research 14, 157–172.

Stelfox, C.E., Burkill, P.H., Edwards, E.S., Harris, R.P., Sleigh, M.A., 1999. The structure of zooplankton communities, in the 2–2000 mu m size range, in the Arabian Sea during and after the SW monsoon, 1994. Deep-Sea Research II 46, 815–842.

Swathi, P.S., Sharada, M.K., Yajnik, K.S., 2000. A coupled physical-biological-chemical model for the Indian Ocean. Proceedings of the Indian Academy Science-Earth and Planetary Science 109, 503–537.

Takeda, S., Kamatani, A., Kawanobe, K., 1995. Effects of nitrogen and iron enrichments on phytoplankton communities in the northwestern Indian Ocean. Marine Chemistry 50, 229–241.

Tarran, G.A., Burkill, P.H., Edwards, E.S., Woodward, E.M.S., 1999. Phytoplankton community structure in the Arabian Sea during and after the SW monsoon, 1994. Deep-Sea Research II 46, 655–676.

Unger, D., Ittekkot, V., Schafer, P., Tiemann, J., Reschke, S., 2003. Seasonality and interannual variability of particle fluxes to the deep Bay of Bengal: influence of riverine input and oceanographic processes. Deep-Sea Research II 50, 897–923.

Uz, B.M., Yoder, J.A., Osychny, V., 2001. Pumping of nutrients to ocean surface waters by the action of propagating planetary waves. Nature 409, 597–600.

Veldhuis, M.J.W., Kraay, G.W., VanBleijswijk, J.D.L., Baars, M.A., 1997. Seasonal and spatial variability in phytoplankton biomass, productivity and growth in the northwestern Indian Ocean: the southwest and northeast monsoon, 1992–1993. Deep-Sea Research I 44, 425–449.

Vinayachandran, P.N., Chauhan, P., Mohan, M., Nayak, S., 2004. Biological response of the sea around Sri Lanka to summer monsoon. Geophysical Research Letters 31, doi:10.1029/2003GL018533.

Vinayachandran, P.N., Saji, N.H., Yamagata, T., 1999. Response of the Equatorial Indian Ocean to an unusual wind event during 1994. Geophysics Research Letters 26, 1613–1616.

Vinayachandran, P.N., Yamagata, T., 1998. Monsoon response of the sea around Sri Lanka: generation of thermal domes and anticyclonic vortices. Journal of Physical Oceanography 28, 1946–1960.

Wang, X., Christian, J.R., Murtugudde, R., Busalacchi, A.J., 2006. Spatio-temporal variability in new production in the equatorial Pacific during 1980–2003: physical and biogeochemical controls. Deep-Sea Research II, this volume [doi:10.1016/j.dsr2.2006.01.023].

Wiggert, J.D., Hood, R.R., Banse, K., Kindle, J.C., 2005. Monsoon-driven biogeochemical processes in the Arabian Sea. Progress in Oceanography 65, 176–213.

Wiggert, J.D., Jones, B.H., Dickey, T.D., Weller, R.A., Brink, K.H., Marra, J., Codispoti, L.A., 2000. The northeast monsoon's impact on mixing, phytoplankton biomass and nutrient cycling in the Arabian Sea. Deep-Sea Research II 47, 1353–1385.

Wiggert, J.D., Murtugudde, R.G., McClain, C.R., 2002. Processes controlling interannual variations in wintertime (Northeast Monsoon) primary productivity in the central Arabian Sea. Deep-Sea Research II 49, 2319–2343.

Wirth, A., Willebrand, J., Schott, F., 2002. Variability of the Great Whirl from observations and models. Deep-Sea Research II 49, 1279–1295.

Wishner, K.F., Gowing, M.M., Gelfman, C., 1998. Mesozooplankton biomass in the upper 1000 m in the Arabian Sea: overall seasonal and geographic patterns, and relationship to oxygen gradients. Deep-Sea Research II 45, 2405–2432.

Yoder, J.A., Moore, J.K., Swift, R.N., 2001. Putting together the big picture: remote-sensing observations of ocean color. Oceanography 14, 33–40.

Young, D.K., Kindle, J.C., 1994. Physical processes affecting availability of dissolved silicate for diatom production in the Arabian Sea. Journal of Geophysical Research 99, 22619–22632.